High-precision geochronology of the Xiaojiayingzi Mo skarn deposit: Implications for prolonged and episodic hydrothermal pulses

Hegen Ouyang[1*], Sean P. Gaynor[2], David Selby[3, 4], Jingwen Mao[1], Qihai Shu[5], Chao Li[6]

[1] MNR Key Laboratory of Metallogeny and Mineral Assessment, Institute of Mineral Resources, Chinese Academy of Geological Sciences, Beijing, 100037, China

[2] Department of Earth Sciences, University of Geneva, 1205 Geneva, Switzerland

[3] Department of Earth Sciences, Durham University, DH1 3LE Durham, UK

[4] State Key Laboratory of Geological Processes and Mineral Resources, China University of Geosciences, Wuhan 430074, China

[5] State Key Laboratory of Geological Processes and Mineral Resources, School of Earth Sciences and Resources, China University of Geosciences, Beijing 100083, China

[6] National Research Center for Geoanalysis, Beijing 100037, PR China

*Corresponding author. E-mail: oyhg1984@163.com

Abstract

The timescales and duration of ore-forming processes in skarn systems are not well constrained. To better understand this, we present high-precision chemical abrasion-isotope dilution-thermal ionization mass spectrometry (CA-ID-TIMS) U-Pb zircon and isotope dilution-negative-thermal ionization mass spectrometry (ID-N-TIMS) Re-Os molybdenite geochronology of the Xiaojiayingzi Mo skarn deposit (0.13 Mt Mo @ 0.22 wt. %), northeastern China. The Xiaojiayingzi deposit is related to an intrusive complex composed of gabbroic diorite, monzodiorite, and granite porphyry. Molybdenite mineralization occurred in two ore blocks, Xiaojiayingzi (0.11 Mt Mo) and Kangzhangzi (0.02 Mt Mo). In the Kangzhangzi ore block, Mo mineralization is concentrated in skarn adjacent to a deep-seated granite porphyry, with minor disseminated and quartz veinlet mineralization within the granite porphyry. In contrast, economic Mo mineralization in the Xiaojiayingzi ore block is concentrated to skarns located between the contact of steeply dipping monzodiorite and the Mesoproterozoic Wumishan Formation, with minor Mo mineralization found in quartz and endoskarn veins hosted in the monzodiorite. Skarn mineralization in both ore blocks converges downward into the mineralized granite porphyry. In the Kangzhangzi ore block, skarn is zoned from deep proximal dark red-brown garnet to shallow distal dark green pyroxene. In the Xiaojiayingzi ore block, proximal skarn is garnet-rich whereas pyroxene increases away from the monzodiorite - Wumishan Formation contact. In addition, pyroxene becomes more Fe- and Mn-rich with distance from the intrusions; Pb, Zn, and Ag increase toward the top of the system, and Mo and Fe increase with depth.

High-precision CA-ID-TIMS U-Pb zircon geochronology indicates the gabbroic diorite crystallized at 165.359 ± 0.028/0.052/0.18 Ma (uncertainties presented as analytical /+ tracer /+ decay constant uncertainties), with subsequent crystallization of the monzodiorite and granite porphyry at 165.361 ± 0.040/0.059/0.19 Ma and 165.099 ± 0.026/0.051/0.18 Ma, respectively. High-precision ID-N-TIMS Re-Os molybdenite geochronology indicates molybdenite mineralization at Xiaojiayingzi occurred in at least three discrete magmatic-hydrothermal pulses (nominally between 165.48 ± 0.09 - 165.03 ± 0.13 Ma , 163.73 ± 0.09 Ma, and 163.11 ± 0.11 Ma). The first episode of molybdenite mineralization formed in exoskarns, endoskarns, and quartz veins, and had a minimum duration of 450 ± 40 kyr, between 165.48 ± 0.09/0.68/0.85 Ma and 165.03 ±

0.13/0.67/0.85 Ma. It is likely that skarn ore represents a composite series of mineralization events, more than the three events capable of identification within analytical uncertainty of these high-precision data. Finally, Re-Os dating of quartz-Mo veins cutting the monzodiorite and granite porphyry indicates that some mineralization postdated the observed intrusions, between 163.73 ± 0.09/0.70/0.86 Ma and 163.11 ± 0.11/0.70/0.86 Ma, interpreted to be the result of deeper, unobserved intrusions. Collectively, these ages indicate that protracted, pulsed Mo mineralization at the Xiaojiayingzi deposit occurred over a time period of at least 2.4 Myrs. These data suggest that individual magmatic and/or skarn garnet ages may significantly underestimate the full duration of mineralization. In addition, this study highlights systematically identify skarn deposits associated with multiphase intrusive systems may be a target for future exploration as it may point to previously undiscovered mineral resources.

Introduction

Skarn deposits are one of the most common ore types in the Earth's crust and are mined for a variety of metals, including Cu, Au, Fe, W, Sn, Mo, Pb, and Zn (Meinert et al., 2005; Chang et al., 2019; Mao et al., 2019). Existing models commonly invoke magma bodies as the source(s) of the fluid, metals, and heat needed to generate skarn deposits, however the lack of close proximity between many skarn deposits and their causative intrusion(s) complicates the relationship between the two, which is crucial to better understand the formation of skarn systems and better target them for economic extraction.

Recent technical advancements in chemical abrasion isotope dilution thermal ionization mass spectrometry (CA-ID-TIMS) have led to improved analytical precision for individual zircons analyses (e.g., 0.01% on a single zircon $^{206}Pb/^{238}U$ age; Widmann et al., 2019; Schaltegger et al., 2021). As a result, this method has been employed in recent studies of the lifespan of upper crustal magma systems and indicates that individual shallow intrusions or intrusive systems, particularly those associated with porphyry mineralization, commonly have very short assembly periods of 10's to 100's of kyr (e.g., Leuthold et al., 2012; Barboni and Schoene, 2014; Eddy et al., 2016; Buret et al., 2017; Gaynor et al., 2019a; Large et al., 2020, 2021; Rosera et al., 2021). These observations only speak to the magmatic processes potentially associated with ore deposits; after fluid exsolution, hydrothermal processes control the spatiotemporal development of ore deposits. Thus, it is crucial to better integrate these observations into understanding the lifespan of individual pulses of mineralization and broader mineral systems. Directly comparing the timing of mineralizing magmas and mineralization events has the potential to reveal the true relationships between magmatism and mineralization. Recent work has begun to investigate the full evolution of magmatic-hydrothermal systems related to porphyry ore deposition by comparing high-precision geochronology of U-Pb zircon and Re-Os molybdenite, which has the possibility of yielding detailed records of the full lifespan of a deposit, from magma emplacement to hydrothermal ore precipitation (e.g., Rosera et al., 2013; Li et al., 2017; Gaynor et al., 2019b; Feely et al., 2020). In these porphyry environments, researchers have increasingly recognized the short-lived nature of individual magmatic-hydrothermal systems, such that many individual magmatic-hydrothermal systems are juxtaposed one to another resulting in metal enrichment (e.g., Li et al., 2017; Gaynor et al., 2019b; Zhao et al., 2021). Due to the common lack of proximity between causative intrusions and dateable ore mineral phases in skarn deposits, there is a scarcity of work examining similar relationships in skarn deposits. Therefore, there is a suite of outstanding questions regarding skarn ore formation, such as: (1) How do large to giant skarn deposits form? (2) How long does it take a major skarn deposit to form? (3) Is the endowment of a skarn deposit formed by a single pulse of magmatic-hydrothermal activity or through episodic enrichment from multiple pulses?

The Xiaojiayingzi Mo skarn deposit is located in the northern part of the North China Craton (Fig. 1). Exploration of the Xiaojiayingzi deposit began in the 1950's, with mining of Pb, Zn, and Ag from carbonate-replacement orebodies. The first systematic exploration campaign occurred between 1975-1979, and led to the discovery of concealed Mo and Fe skarn orebodies at the contacts between the dioritic intrusion and carbonate rock in the Xiaojiayingzi ore block (Figs, 2, 3a), and yielded a resource of 0.11 Mt Mo at an average grade of 0.23 wt. % and 8.87 Mt Fe at an average grade of 33.4 wt. % (Gao et al., 1979). More recently, exploration has led to the discovery of porphyry and skarn mineralization in the Kangzhangzi ore block, spatially related to a deep, unexposed granite porphyry (Figs. 3b, 4), which yields an additional resource of 0.02 Mt Mo at 0.118% and 1.14 Mt Fe at 26.5% (Guan et al., 2010). Exploration is still ongoing. Therefore, given how new exploration campaigns have led to significant ore discoveries over half a century since initial mining, detailed study of the Xiaojiayingzi Mo deposit may help improve existing models of skarn deposit formation. Although the geology of the Xiaojiayingzi deposit remains poorly constrained, particularly at depth, recent drilling has revealed critical magmatic, hydrothermal, and structural relationships.

We examined field relationships between the various intrusions of the Xiaojiayingzi deposit, documenting alteration and mineralization relationships, and integrated new high-precision U-Pb zircon and Re-Os molybdenite geochronology to better understand the formation of the Xiaojiayingzi deposit. Our purposes are to (1) characterize magmatism, alteration, and mineralization, (2) document the spatial distribution of alteration and mineralization, (3) constrain the time of magmatism and mineralization, and (4) discuss the relationship of the magmatic and hydrothermal processes. Using these data, we reevaluate the formation of the Xiaojiayingzi deposit and the controls on the spatial distribution of skarn mineralization from local magmatism.

Furthermore, these data also provide insight into the metasomatism stages through time in skarn systems and highlight the key role of successive magmatic fluid injection in the formation of large skarn deposits.

Geological Background

Regional geology

The Xiaojiayingzi deposit is located in western Liaoning, North China Craton (Fig. 1a), and is part of an EW-trending belt of Jurassic to Cretaceous deposits known as the "Yanshan-Liaoning Mo-Au metallogenic belt" (Li et al., 2012; Zeng et al., 2013). The basement of western Liaoning is composed of Archean to Paleoproterozoic greenschist- to granulite-facies metamorphic rocks, largely tonalite - trondhjemite - granodiorite (TTG) gneiss, amphibolite, migmatite, and ultramafic rocks, which were metamorphosed during the collision between the western and eastern North China cratons at ca. 1.85 Ga (Zhao et al., 2001). From the late Paleoproterozoic to the early Paleozoic, western Liaoning received frequent deposition of shallow-marine carbonate platform sediments (Yang et al., 1986). Since the late Paleozoic, western Liaoning was affected by multiple orogenic events, especially during the Late Permian to late Mesozoic. The first event was thrusting and crustal thickening around the north margins of North China Craton during the closure of the Paleo-Asian Ocean at the Late Permian to Early Jurassic time (Xiao et al., 2003). The second event was the destruction of the North China Craton during the Late Jurassic to Early Cretaceous (Menzies and Xu, 1998; Zhu et al., 2011), which coincided with a major change in subduction direction of the Paleo-Pacific plate (Sun et al., 2007) and with the formation of intracontinental rift basins, metamorphic core complexes, and bimodal volcanic rocks in the North China Craton (Ren et al., 2002; Liu et al., 2005; Zhu et al., 2011).

Western Liaoning hosted episodic voluminous, felsic magmatism, with lesser amounts of mafic to intermediate magmatism, contemporaneous with these orogenic events (Fig. 1b). Four pulses of magmatism have been identified in western Liaoning: (1) rare Late Triassic (ca. 221 Ma) intermediate intrusions and trachyandesitic to rhyolitic volcanic rocks, (2) voluminous Early Jurassic (190 - 180 Ma) granitic plutons and high-Mg andesites and dacites, (3) less voluminous Middle to Late Jurassic (170 - 150 Ma) basalt to rhyolite complexes, and (4) minor Early

Cretaceous mafic to felsic intrusions and basaltic to andesitic (high-Mg) volcanic rocks (Wu et al., 2006; Yang and Li, 2008; Ma et al., 2012; Zhang et al., 2014). Early Jurassic intrusions, which usually occur as batholiths (Fig. 1b, Wu et al., 2006), were formed by mixing of crustal- and enriched mantle-derived magmas (Zhang et al., 2014) and are spatially related to important Mo deposits (Ouyang et al., 2013, 2020; Shu et al., 2016).

Regional deformation in western Liaoning was characterized by NS-trending compressional structures during the Early to Middle Triassic but transformed to NS extension during the Late Triassic to Early Jurassic (Zhang et al., 2014). The Middle Jurassic to Early Cretaceous deformation does not have a consistent orientation, indicating that various tectonic regimes may have occurred during that period (Zhang et al., 2014). The fourth deformation event was during the Early Cretaceous and involved NW-SE extension, likely related to the far-field effect of Paleo-Pacific plate subduction or post-subduction (Yang and Li, 2008; Li et al., 2012; Zhang et al., 2014; Mao et al., 2021).

Several medium- (0.01 to 0.10 Mt) to large- (≥ 0.10 Mt; Chinese national Standard GB/T 17766-1999) porphyry-skarn Mo deposits occur in western Liaoning, including Yangjiazhangzi, Lanjiagou, Songbei, Xintaimen, and Xiaojiayingzi (Fig. 1b). Molybdenum mineralization at many of these deposits is either hosted in or is associated with Early Jurassic felsic intrusions (Ouyang et al., 2020 and references therein), and mineralization occurred over a relatively narrow time interval (187 - 183 Ma; Ouyang et al., 2013 and references therein). This is not always the case, as previous work has suggested that Mo mineralization at Xiaojiayingzi occurred at approximately 165 Ma (Dai et al., 2009), and therefore represents a separate mineralization event in western Liaoning. Moreover, in terms of surface expression, the Xiaojiayingzi deposit has been interpreted to be the result of a mafic to intermediate intrusive complex (Gao et al., 1979; Dai et al., 2009), in contrast to the other porphyry to skarn Mo deposits in the district and elsewhere in the world.

District geology

In the Xiaojiayingzi district, an Archean metamorphic complex composed mostly of gneiss and amphibolite is exposed northwest of the Zhongsanjia and Chengde-Beipiao faults (Fig. 2a). Early Jurassic granitic plutons intrude the metamorphic complex, but are only exposed northwest of these faults (Yu et al., 2014). To the southeast of the Chengde-Beipiao fault, the Archean metamorphic complex is unconformably overlain by a thick calcareous sequence (up to 4000 m in thickness) of the Mesoproterozoic Wumishan Formation, composed of carbonate rocks with lenses of calcareous shale, calcareous siltstone, and sandstone, and the succession represents a peritidal carbonate deposit (Zhao et al., 2001). The carbonate rocks are well bedded and contain variable CaO (20 - 53 wt. %) and MgO (0.5 - 32 wt. %; Zhao et al., 1990). In some carbonate rock beds, there are abundant chert bands and nodules. The Wumishan Formation is unconformably overlain by late Mesozoic volcanic rocks, and is intruded by the Triassic and Middle Jurassic mafic to intermediate intrusions associated with Mo and Cu mineralization (Fig. 2a; Dai et al., 2009; Yu et al., 2014).

Several Mo, Cu-Mo, and Au deposits and prospects exist in the Xiaojiayingzi district, including the Xiaojiayingzi Mo deposit, the Didashui, Chabucha, Shuitanggou, and Sandaogou Cu-Mo prospects, and the Zhongsanjia Au deposit (Fig. 2a). The Zhongsanjia Au deposit is located northwest of the Zhongsanjia and Chengde-Beipiao faults. Lode gold veins in this deposit are hosted in Archean TTG gneiss and amphibolite, and have no clear association with intrusive rocks (Gao et al., 1979). In contrast, the Mo and Cu-Mo skarn deposits or prospects are confined to the Wumishan Formation southeast of the Chengde-Beipiao fault (Fig. 2a). Furthermore, they are largely associated with a Middle Jurassic mafic to intermediate igneous complex, which intruded into the Wumishan Formation (Dai et al., 2009; Yu et al., 2014).

There are three main sets of faults in the Xiaojiayingzi district. The first set, represented by the near EW-trending Chengde-Beipiao deep fault, extends for tens of kilometers throughout the district. It is a regional-scale thrust and is generally parallel to the Chifeng-Kaiyuan suture, which connects the North China Craton and Central Asian Orogenic Belt (Fig. 1a; Xiao et al., 2003). The second set of faults, which strikes NE, is part of a regional strike-slip system. They commonly significantly offset stratigraphy, earlier EW-trending faults and Triassic intrusions (Fig. 2a). The third set of faults strikes NW. Middle Jurassic intrusions, and their associated alteration and mineralization, typically occur at junctions between the NE- and NW-trending faults, or along the NW-trending faults (Fig. 2a).

Previous Studies

The Xiaojiayingzi deposit consists of the Xiaojiayingzi and Kangzhangzi ore blocks (Figures 2b-3). Skarn mineralization in the Xiaojiayingzi deposit was first reported by Gao et al. (1979). Dai et al. (2009) described the skarn alteration and mineralization in the Xiaojiayingzi ore block, and recognized a skarn zoning as follows: diorite → garnet skarn → garnet - diopside skarn → diopside - forsterite skarn → chondrodite - phlogopite skarn → skarn dolomite → dolomite. Liu et al. (2012) recognized skarn- and vein-types mineralization in the Xiaojiayingzi ore block, and interpreted Xiaojiayingzi as a porphyry-skarn Mo deposit related to a dioritic intrusion. Fluid inclusion data showed that garnets in prograde endoskarn were associated with high-temperature (520°-560°C), high-salinity (44-50 wt % NaCl equiv.) fluids; calcite and quartz associated with retrograde alteration and Mo mineralization were associated with hydrothermal fluids of moderate-salinity (4-18 wt % NaCl equiv.) and temperatures between 320° and 440°C (Dai et al., 2008). Based on oxygen and hydrogen isotope compositions of garnet and calcite, and platinum group elements concentration and sulfur isotope composition of sulfide minerals, Dai et al. (2008, 2013) concluded that the ore-forming fluids of the Xiaojiayingzi deposit were dominantly of magmatic origin, most likely sourced from the dioritic intrusion. However, all these studies are focused on the Xiaojiayingzi ore block, and the geology of the Kangzhangzi ore block has not been described by previous research, particularly at depth, where recent drillings have intersected a mineralized granite porphyry intrusion. Furthermore, the relationship between the Xiaojiayingzi and Kangzhangzi ore blocks, and the genesis of the Xiaojiayingzi skarn mineral system have not been previously described or discussed.

The ages of intrusive rocks in the Xiaojiayingzi deposit have been poorly documented. Two whole-rock K-Ar ages of 177 Ma and 113 Ma from uncharacterized gabbro diorite and diorite samples, respectively, were the primary constraints on the ages of magmatism in the Xiaojiayingzi deposit (Gao et al., 1979). Dai et al. (2009) performed sensitive high-resolution ion microprobe (SHRIMP) zircon U-Pb dating of the diorite intrusion, which yielded a weighted $^{206}Pb/^{238}U$ mean age of 171.2 ± 5.0 Ma (2σ, MSWD = 3.2). Previous dating of the Xiaojiayingzi Mo skarn mineralization includes six molybdenite Re-Os model ages acquired by isotope dilution inductively-coupled plasma mass spectrometry (ID-ICP-MS) method, which range from 165.9 ±

2.8 to 159.1 ± 2.6 Ma (2σ, Dai et al., 2009).

Methods

Field investigation and petrography

In this study, field data of magmatism, mineralization, and alteration were collected largely based on underground mapping, drill core observation, and petrographic observations. Fifty-one representative samples that were collected from underground mine and drill cores (Appendix Table S1) were examined using optical and scanning electron microscopy (Hitachi TM3030) to document the intrusive phases, the vein and related hydrothermal alteration assemblages, and the mineral paragenesis. The temporal evolution of magmatism, alteration, and mineralization in the Xiaojiayingzi mineral system was determined by observing crosscutting relationships between intrusions and veins, variations in alteration and mineralization styles in intrusions and their contiguous host rocks, together with the relative age of veins relative to each other and to intrusions.

Electron microprobe analyses

To constrain the skarn mineral compositions and their spatial variations, skarn samples from the Xiaojiayingzi and Kangzhangzi ore blocks were collected systematically for electron microprobe analyses. We sampled 45 skarn samples that range from endoskarn, proximal massive skarn, and intermediate and distal skarns in both ore blocks. The sample locations and descriptions are provided in Appendix Table S1. Compositions of skarn minerals were obtained on a JEOLJXA-8230 electron microprobe in wavelength-dispersive mode with 15-kV acceleration, 10-nA beam current, and 2-μm spot size at the Institute of Mineral Resources, Chinese Academy of Geological Sciences. Synthetic (i.e., silica for Si and spessartine for Mn) and natural (i.e., sanidine for K, pyrope for Mg, andradite for Fe and Ca, albite for Na and Al, and rutile for Ti) minerals were selected for instrument calibration. The estimated precision for each element is better than ± 2.0 %.

Zircon U-Pb CA-ID-TIMS dating

Samples of the gabbroic diorite (CXJYC), monzodiorite (QXJYC), and granite porphyry (ZJ31-5) from subsurface exposures and drill cores were selected for CA-ID-TIMS zircon U-Pb dating. Detailed sample locations are provided in Appendix Table S1.

After washing, samples were jaw-crushed, disc milled, and sieved. Heavy minerals were concentrated using a Rogers table, then a Frantz electromagnetic separator, and finally by standard heavy liquid (diiodomethane) concentration. Zircon grains from the concentrated materials were then handpicked under a binocular microscope. Once zircon grains had been extracted from the samples, they were annealed in a muffle furnace at 900 °C for 48 hours (Mundil et al. 2004). The annealed grains were chemical abraded at 210 °C for 12 hours in concentrated HF in 3 ml Savillex beakers placed in a Parr digestion vessel (Mattinson 2005; Widmann et al. 2019). The grain fragments remaining after chemical abrasion were then leached on a hotplate at 80 °C in 6 N HCL overnight, followed by further cleaning through four rounds of 7 N HNO_3 in combination with ultrasonication. Individual cleaned zircon crystals were then loaded into individual 200 µlSavillex microcapsules, spiked with the EARTHTIME $^{202}Pb + ^{205}Pb + ^{233}U + ^{235}U$ tracer solution (calibration version 3; McLean et al. 2011; Condon et al. 2015) and dissolved with about 70 µl HF and trace HNO_3 in a Parr digestion vessel at 210 °C for at least 48 hours. Following dissolution, the samples were dried down and converted to a chloride by placing them back in the oven overnight in 6 *N* HCl. The samples were then dried down again and re-dissolved in 3 *N* HCl, and purified to U and Pb through anion exchange column chromatography (Krogh 1973). Once purified, the U and Pb fractions were combined in cleaned 7 ml Savillex beakers and dried down with trace H_3PO_4, prior to loading on outgassed zone-refined Re ribbon filaments with a Si-gel emitter.

Uranium and Pb isotope analyses were completed on an Isotopx Phoenix TIMS machine at the University of Geneva (Switzerland). Lead measurements were made in dynamic mode using a Daly photomultiplier, and U was measured as an oxide in static mode using Faraday cups coupled to 10^{12} Ω resistors. The $^{18}O/^{16}O$ oxygen isotope ratio in uranium oxide was assumed to be 0.00205 based on previous measurements of the U500 standard. Mass fractionation of Pb and U was corrected using a $^{202}Pb/^{205}Pb$ ratio of 0.99506 and a $^{238}U/^{235}U$ ratio of 137.818 ± 0.045 (2σ, Hiess et al. 2012). All common Pb was considered laboratory blank and was corrected using the long-term isotopic composition of the Pb blank at the University of Geneva (Schaltegger et al., 2021). All data were processed with the Tripoli and Redux U–Pb software packages (Bowring et al. 2011; McLean et al. 2011). All ages were corrected for initial ^{230}Th disequilibrium in the melt using a U/Th ratio of the magma of 3.5. Earthtime ET100 standard solution analyzed during the period of these analyses yielded a value of 100.177 ± 0.010 Ma (MSWD = 2.6; n = 8), within uncertainty of the recently reported inter-laboratory calibrated value of 100.173 ± 0.003 Ma for this solution (Schaltegger et al., 2021).

Molybdenite Re-Os isotope dilution negative thermal ionization mass spectrometry (ID-N-TIMS) dating

Three molybdenite-bearing exoskarn samples (XJYZ-1/XJYZ-3/X-1), one molybdenite-bearing endoskarn sample (X-4), one molybdenite-bearing iron ore sample (X-3), two quartz-molybdenite-pyrite±chalcopyrite vein samples hosted in monzodiorite (X-8/X-9), and one quartz-molybdenite-pyrite veinlet sample hosted in granite porphyry (X-6-2) from both underground mine and drill cores, covering all the molybdenum mineralization types in the Xiaojiayingzi mineral system, were sampled for ID-N-TIMS molybdenite Re-Os geochronology. None of the samples show evidence of temperature reversal in their alteration assemblage, in order to avoid the potential of mixing subsequent molybdenite crystallization in with the molybdenite of interest (Appendix Table S2). Detailed sample locations and descriptions are provided in Appendix Table S1-S2.

To avoid any potential disturbance of Re-Os by overprinting and mixing different generations of molybdenite mineralization, samples selected for dating did not exhibit any crosscutting relationships and exhibited the least evidence of alteration or overprint (e.g., Seedorff and Euinadi, 2004). The molybdenite separation method was adopted from previous studies (Lawley and Selby, 2012).

Molybdenite Re-Os isotope analysis was carried out at the Laboratory for Sulfide and Source Rock Geochronology and Geochemistry and the Arthur Holmes Laboratory at Durham University, United Kingdom, members of the Durham Geochemistry Centre. The Re-Os analytical protocol followed Selby and Creaser (2001) and Li et al. (2017). A weighed aliquot of molybdenite and spike solution (^{185}Re plus isotopically normal Os) was loaded into a Carius tube with 11*N* HCl (3 ml) and 15.5*N* HNO_3 (6 ml), sealed and placed in a Carius tube, and digested at 220°C in an oven for ~24 h. Osmium was purified from the acid medium using solvent extraction ($CHCl_3$) at room temperature and microdistillation methods. The rhenium fraction was isolated by sodium hydroxide-acetone solvent extraction and HCl-HNO_3 anion chromatography. The purified rhenium and osmium were loaded onto Ni and Pt filaments, respectively, and their isotopic compositions were measured using ID-N-TIMS (Creaser et al., 1991).

The isotopic analysis was conducted on a Thermo Scientific TRITON mass spectrometer in the Arthur Homes Laboratory at Durham University, with Re and Os isotope compositions measured using the static Faraday collection mode. The uncertainties in the Re and Os concentrations and Re-Os isotope ratios were determined by propagating the spike calibration, the sample and spike weight uncertainty, the reproducibility of Re and Os isotope standard values, and the blank abundances and isotopic compositions that were run alongside the molybdenite analysis. A full analytical protocol blank measured alongside the molybdenite analyses was 3.4 pg for Re and 0.1 pg for Os, with a $^{187}Os/^{188}Os$ composition of 0.20 ± 0.02. Molybdenite Re-Os model ages were calculated using the equation $t = \ln(^{187}Os/^{187}Re + 1)/\lambda$, employing a λ value of $1.666 \times 10^{-11} \pm 5.165 \times 10^{-14}$ a^{-1} (Smoliar et al., 1996). To evaluate the accuracy and reproducibility of the molybdenite Re-Os data, the NIST molybdenite reference material (RM 8599) is routinely analyzed, which yielded an running average age as of September 2021 (date of analysis) of 27.66 ± 0.09 Ma (n = 30), which is in agreement within uncertainty with the recommended age of 27.656 ± 0.022 Ma (Zimmerman et al., 2014).

Results

Xiaojiayingzi deposit geology

Our observations combined with exploration data permit a new detailed reconstruction of the Xiaojiayingzi deposit geology, indicating that the deposit geology is more complex than previously discussed. The details are summarized in the following sections.

Magmatism

Based on crosscutting relationships and mineral modal abundance (IUGS recommendation), three intrusions are identified in the Xiaojiayingzi deposit, which include, in time sequence, gabbroic diorite, monzodiorite, and granite porphyry (Fig. 5a-b). The first two intrusions are by far the most voluminous with an outcrop area of about 0.75 km^2 (Fig. 2b), whereas the granite porphyry has been intersected only by drillings down to approximately 900 m depth below the current ground surface or by underground mining. At deeper levels, all these intrusions merge downward into an intrusive complex (Fig. 4), which is referred to as the Xiaojiayingzi intrusive complex in this study. Surrounding the Xiaojiayingzi intrusive complex is the carbonate wall rocks of the Wumishan Formation. The characteristics of the Xiaojiayingzi intrusive complex are summarized in Table 1.

The gabbroic diorite (Fig. 5c) is one of the major intrusions of the Xiaojiayingzi intrusive complex with an outcrop area of 0.3 km^2. It occurs as a stock intruding into the Wumishan Formation and was in turn truncated by the monzodiorite along its south and east flanks (Fig. 2b). The western extent of the gabbroic diorite is obscured by cover rocks and its overall dimension is unknown. The gabbroic diorite is distinguished from other intrusions by its dark color and coarse texture (Fig. 5c). Major minerals include variable proportions of plagioclase (55 - 65 vol. %), biotite (10 - 15 vol. %), and hornblende (5 - 10 vol. %), which constitute 90 vol. percent of the rock, accompanied by 5 to 10 vol. percent of augite (Fig. 5d). Accessory phases comprise apatite, ilmenite, magnetite, titanite, and zircon (Fig. 6c-d; Appendix Figure 1a). Locally, barren quartz veinlets with K-feldspar and epidote envelopes, and quartz - pyrite ± galena ± sphalerite ± chalcopyrite and molybdenite veinlets with sericite ± epidote envelopes crosscut the gabbroic diorite (Fig. 6). Nonetheless, the gabbroic diorite is poorly mineralized.

In plan view, the monzodiorite (Fig. 5e) is exposed as stocks or dikes intruding into the gabbroic diorite and the Wumishan Formation (Fig. 2b; Appendix Figure 2a), with an outcrop area of about 0.45 km^2. It has many irregular contacts and apophyses into the Wumishan Formation (Figs. 3-4), and hosts some (dolomitic) limestone xenoliths, especially near its border. The monzodiorite is medium-grained and two textural varieties were identified, one dark-gray and equigranular, and the other gray and equigranular to porphyritic (Fig. 5b). Contacts between the two phases are commonly gradational and no crosscutting relationships were observed in this study. The monzodiorite is composed of 55 to 60 vol. % plagioclase, 10 to 15 vol. % alkaline feldspar, 10 to 15 vol. % biotite, and 5 to 10 vol. % hornblende with minor amounts of quartz (< 5 vol. %) and augite (< 1 vol. %) (Fig. 5f); accessory minerals include apatite, ilmenite, magnetite, zircon, and titanite (Appendix Figure 1b). Where the intrusion is porphyritic, plagioclase phenocrysts in the monzodiorite range in size from 3 to 10 mm (Fig. 3e). At Xiaojiayingzi, the monzodiorite is the most significant intrusion in terms of the volume of quartz - molybdenite - pyrite ± galena ± sphalerite ± chalcopyrite veining it hosts (5 - 10 vol. %; Table 1; Fig. 7b-f) and is one of several important hosts for molybdenite mineralization. The monzodiorite also has mineralized garnet-pyroxene endoskarn on a scale of meters near some contacts with the exoskarn (Fig. 7a).

The granite porphyry (Fig. 5g), which displays weak to intense potassic and sericitic alteration (Fig. 8), is found in drill core from the Kangzhangzi ore block or by underground mining in the Xiaojiayingzi ore block, and was not reported in previous studies. It occurs as stocks or dikes, truncates the gabbroic diorite and monzodiorite (Fig. 5a-b), and intrudes the Wumishan Formation (Appendix Figure 2b; Fig. 4). These observations indicate the granite porphyry is likely the latest intrusion of the Xiaojiayingzi intrusive complex. The granite porphyry contains variable proportions of alkaline feldspar (30 – 40 vol. %) and quartz (10 – 15 vol. %) phenocrysts, accompanied by minor plagioclase (< 5 vol. %) and biotite (< 1 vol. %) phenocrysts set in a microcrystalline matrix of quartz (30 - 35 vol. %), alkaline feldspar (~5 vol. %), plagioclase (< 2 vol. %), and biotite (< 2 vol. %); accessory minerals include zircon, apatite, and magnetite (Table 1). The alkaline feldspar and quartz phenocrysts in the granite porphyry unit are usually very large (up to 30 mm), whereas the plagioclase and biotite phenocrysts are always smaller (< 3 mm; Fig. 5g-h). The groundmass tends to become coarse with depth, with the texture eventually becoming seriate, then porphyritic with a hypidiomorphic-granular matrix, and finally granitic at deeper levels. Correspondingly, the granite porphyry grading from light pink to gray-white with depth, possibly related to a decrease in the content of pinkish orthoclase and/or in the hydrothermal alteration intensity. The granite porphyry was affected by quartz ± biotite ± molybdenite ± pyrite veining (Fig. 8), but the abundance is generally low (2 - 5 vol. %; Table 1).

Alteration and distribution

Four main types of hydrothermal alteration assemblages are identified within the Xiaojiayingzi mineral system in this study: sodic, potassic, sericitic, and skarn alteration. Sodic alteration is only observed in the monzodiorite, and is characterized by primary plagioclase altered to white albite, and hornblende and biotite to chlorite, which were then overprinted/crosscut by later endoskarn (Fig. 7a). No molybdenite mineralization is observed in this alteration stage.

Potassic alteration is represented by the replacement of primary plagioclase by K-feldspar. Two types were observed: disseminated and veining. The disseminated potassic alteration is characterized by primary plagioclase being pervasively altered to K-feldspar (Fig. 8b, 8h), and is only observed in the granite porphyry. The veining type potassic alteration is characterized by the formation of secondary K-feldspar in or around quartz veinlets (Fig. 6a), quartz-molybdenite-pyrite vein (Fig. 7b) or quartz - biotite veinlets (Fig. 8b-c). It is relatively well developed in the monzodiorite and granite porphyry, but is rare in the gabbroic diorite. In the monzodiorite, potassic alteration is more intense in areas proximal to the contacts with the Wumishan Formation and is associated with molybdenite mineralization (Fig. 7a-b). It represents one of several important molybdenite mineralization-related alteration types in the Xiaojiayingzi system. In the granite porphyry, potassic alteration is more intense in the apical part of the intrusion, especially in areas proximal to the contacts with the Wumishan Formation, but becomes less intense with depth due to the decrease in the abundance of veining. No molybdenite mineralization was introduced during this alteration stage in the granite porphyry.

Sericitic alteration is characterized by the replacement of plagioclase by fine-grained muscovite, accompanied by a small percentage of disseminated pyrite along quartz - molybdenite ± pyrite ± chalcopyrite ± galena ± sphalerite veins (Figs. 7c-f, 8b, 8d-e, 8h) or quartz-pyrite veins and veinlets (Figs. 6a-b, 8d, 8h). It affects all the intrusions of the Xiaojiayingzi intrusive complex. In the granite porphyry, sericitic alteration commonly overprints the earlier potassic alteration (Fig. 8b, 8h), and represents the main molybdenite mineralization-related alteration type in this intrusion.

Skarn alteration in the Xiaojiayingzi deposit is extensive but varies with rock type, and represents the most important molybdenite mineralization-related alteration type. Generally, this type of alteration is pervasive in the Wumishan Formation, especially in areas peripheral to the monzodiorite and granite porphyry, in the form of exoskarn (Figs. 3-4). Skarn alteration is also observed in the monzodiorite as endoskarn (Fig. 7a), but is less common. The exoskarn hosts the bulk of the Xiaojiayingzi orebodies, but the ratios of garnet and pyroxene, and of economic minerals (e.g., molybdenite and magnetite) in the exoskarn assemblages are varied with the protoliths of the Wumishan Formation. Two exoskarn assemblages are recognized, including Mg and Ca exoskarns.

The Mg exoskarns are characterized by prograde pyroxene and minor garnet, and retrograde phlogopite, magnetite, actinolite, and calcite, with minor amount of molybdenite, chalcopyrite, and pyrite (Fig. 9). The Mg exoskarns are associated with iron mineralization. In the Xiaojiayingzi ore block, Mg exoskarns tend to be massive and occur proximal to the contact between the steeply dipping monzodiorite and the Wumishan Formation (Fig. 3a). In the Kangzhangzi ore block, Mg exoskarns are well developed in areas near the contact between the granite porphyry and the overlying Wumishan Formation as massive and stratiform skarns (Figs. 3b, 4). Pyroxene crystals in the Mg exoskarns are dark green in color with an average composition of Di(diopside)$_{51}$Hd(hedenbergite)$_{45}$Jo(johannsenite)$_{5}$ (Appendix Table S3). Retrograde alteration, consisting dominantly of magnetite, phlogopite, and actinolite, overprinted the Mg exoskarns (Fig. 9a-b), and in extreme circumstance, almost completely obliterates the prograde pyroxene (Fig. 9c-e). Locally, calcite, chalcopyrite, pyrite, molybdenite, and galena are present as well, but are less common opaque phases, and generally postdating magnetite mineralization (Fig. 9c-f).

The Ca exoskarns consist of prograde garnet and pyroxene, and retrograde molybdenite, calcite, and actinolite, with minor amount of chalcopyrite (Fig. 10). The Ca exoskarns host the bulk of the Mo orebodies. In the Xiaojiayingzi ore block, the Ca exoskarns are most widely developed proximal to the contact between the monzodiorite and the Wumishan Formation in the form of massive skarns, and extend for variable distances into the Wumishan Formation laterally as skarn veins (Fig. 3a). In contrast, the Ca exoskarns in the Kangzhangzi ore block are well developed next to the contact between the granite porphyry and the Wumishan Formation, and extend vertically to distal locations along bedding planes or faults in the Wumishan Formation (Figs. 3b-4). The Ca exoskarns also occur inside the monzodiorite as replacement of limestone xenoliths by garnet and pyroxene with grayish halos consisting of epidote and chlorite, but are less common. In the Ca exoskarns, garnet is commonly rimmed by molybdenite and calcite (Fig. 10); pyroxene is altered to dark green actinolite (Fig. 10a, 10c), and then is crosscut by quartz veinlets (Fig. 10e-f).

As with many skarn systems (Meinert, 1997) the garnet/pyroxene ratios and color of the Ca exoskarns in the Xiaojiayingzi deposit are zoned in space relative to their distance to intrusions of the Xiaojiayingzi intrusive complex. In the Xiaojiayingzi ore block, the Ca exoskarns in zones proximal to the monzodiorite are generally massive, coarse-grained, and garnet-rich (consisting of over 85 vol % garnet). The garnet is commonly coarse-grained (up to 11 cm in size), optically zoned, and has a dark red-brown color, whereas pyroxene in this zone is pale in color (Fig. 10). Retrograde alteration (mostly actinolite) and sulfide minerals (mostly molybdenite) are abundant in those proximal Ca exoskarns. From the monzodiorite - Wumishan Formation contact to the east, the garnet content in the Ca exoskarns decreases, whereas pyroxene generally increases (Fig. 3a; Appendix Figure 3). In the Kangzhangzi ore block, the garnet/pyroxene ratios and color of the Ca exoskarns is zoned vertically relative to the granite porphyry - Wumishan Formation contact. From the granite porphyry - Wumishan Formation contact upward to the distal zones, there is a trend of increasing pyroxene in the Ca exoskarns (Fig. 4). Accompanying this change, the color of garnet changes from proximal dark red-brown, through brown in intermediate zones, to yellow and pale green in distal zones, whereas the color of pyroxene changes from proximal pale green to dark green in distal locations.

Compositionally, there is little or no correlation between the relative distance to the Xiaojiayingzi intrusive complex and the major element composition of garnets in both of the Xiaojiayingzi and Kangzhangzi ore blocks. As shown in Figure 11a, proximal garnets from both of the Xiaojiayingzi and Kangzhangzi ore blocks exhibit a wide range of composition (ranging from $Gro(grossular)_{77}And(andradite)_{21}$ to $Gro_{18}And_{75}$). In individual crystals, the proximal garnet displays Fe enrichment from core to rim (Appendix Figure 4). Intermediate and distal garnets show compositions ranging from $Gro_{72}And_{21}$ to $Gro_{5}And_{89}$, comparable to those from the proximal zones (Fig. 11a). Unlike garnet, the composition of pyroxene is zoned within the Xiaojiayingzi mineral system. As shown in Figure 4 and Figure 11b, proximal pyroxenes from both of the Xiaojiayingzi and Kangzhangzi ore blocks are Fe-poor, with compositions ranging from pure diopside to $Di_{52}Hd_{47}Jo_{1}$. Intermediate and distal pyroxenes are Fe-rich, with mole percentage of hedenbergite between 41 to 94% (71 % on average). In addition, proximal pyroxenes are Mn-poor (4 mole percent johannsenite on average), whereas the intermediate and distal pyroxenes are Mn-rich (7 mole percent johannsenite on average), possibly suggesting that the metasomatic fluid was Mn-poor by the time of initial skarn formation and then was progressively enriched in Mn as the skarn evolved.

The endoskarn in the monzodiorite occurs commonly as veins 1 to 5 cm in width (Fig. 7a). Locally, the veins can be wider (up to 30 cm) where more veins intersect. The endoskarn veins are dominated by red-brown garnet with variable of pyroxene, molybdenite, pyrite, and chalcopyrite. Generally, there is more pyroxene where the veins are wider (Fig. 7a), but even in the most pyroxene-rich veins, pyroxene is less abundant than garnet. The garnet in the endoskarn is uniformly andraditic in composition ($Gro_{8-36}And_{58-85}$; Fig. 11a). Pyroxene belongs to the diopside-hedenbergite series ($Di_{18-90}Hd_{8-80}Jo_{1-6}$; Fig. 11b). Moreover, the garnet is relatively more Al-rich in narrow veins without Mo mineralization ($Gro_{20-36}And_{58-76}$) and more Fe-rich in wide, Mo-mineralized veins ($Gro_{8-29}And_{66-85}$; Appendix Table S3). The endoskarn is intensively mineralized; however, only approximately 5 % of the total Mo resource was deposited during this sub-type of skarn alteration (Guan et al., 2010).

Mineralization and distribution

In the Xiaojiayingzi deposit, molybdenite and magnetite are the two minerals present in economic proportions, although minor amounts of chalcopyrite, galena, sphalerite, Ag-bearing minerals, and bismuthinite are also present. In plan view, mineralization in the Xiaojiayingzi deposit occurs as skarns at the southern and eastern margins of the monzodiorite (Fig. 2b). Geological cross-sections from the Xiaojiayingzi ore block show that the bulk of mineralization in this ore block developed at the contact between the monzodiorite and the Wumishan Formation, where more than 80 skarn orebodies are located, down to depths of approximately ca. 800 m below the current surface (Fig. 4a). In contrast, drill core data from the Kangzhangzi ore block show that economic mineralization in this ore block is well developed around the granite porphyry in the form of skarn down to depths of more than 1,200 m below the current surface (Figs. 4b, 5). Beyond the limit of skarn, Pb, Zn, and Ag show enrichment toward the distal locations relative to the monzodiorite and granite porphyry (up to 0.54 % Pb and 1.5 % Zn; Guan et al., 2010). In this study, three main styles of mineralization were observed, including porphyry Mo, skarn Mo and Fe, and carbonate-replacement Pb-Zn-Ag mineralization. The details are described below.

Porphyry-style Mo mineralization consists of veinlet-hosted, disseminated, and vein-hosted mineralization. The former two occur as quartz - molybdenite ± pyrite veinlets with sericitic halos (typically less than 2 mm in width; Fig. 8b, 8d-e, 8h), and disseminated molybdenite and chalcopyrite along the grain boundaries of the alkaline feldspar phenocrysts (Fig. 8f-g), respectively, in the granite porphyry. In general, the veinlet-hosted mineralization is well developed in the shallow levels of the granite porphyry. At depth, mineralization is dominated by disseminated molybdenite and chalcopyrite. However, the average Mo and Cu grades in the granite porphyry are generally less than 0.04 wt. % and 0.5 wt. %, respectively (Guan et al., 2010). Vein-hosted mineralization is characterized by quartz - molybdenite - pyrite veins 0.5 to 4 cm in width with K-feldspar halos (Fig. 7b) or by quartz - molybdenite - pyrite - chalcopyrite - galena - sphalerite veins up to 7cm in width with sericitic envelopes (Fig. 7c-e), which were overprinted by later coarse-grained pyrite and fluorite (Fig. 7f). This type of porphyry-style mineralization is only observed in the monzodiorite near the Wumishan Formation and generally has a high Mo grade (locally contains up to 0.2 wt. % Mo). However, only about 5 - 10 % of the total Mo resource in the Xiaojiayingzi deposit was deposited in this type of porphyry-style mineralization (Guan et al., 2010).

Skarn-style Mo and Fe mineralization in the Xiaojiayingzi deposit is dominantly developed in the Wumishan Formation in the form of exoskarn (approximately 85 - 90 % of the total Mo resource and 100 % of the total Fe; Guan et al., 2010). Endoskarn veins 0.5 to 5 cm in width hosted in the monzodiorite form a less significant expression of mineralization (Fig. 7a). The exoskarn mineralization can be further subdivided into three sub-types: (1) massive exoskarn mineralization, (2) stratiform exoskarn mineralization, and (3) vein-type exoskarn mineralization. Massive exsoskarn is most commonly present adjacent to the monzodiorite and granite porphyry; minor amounts are hosted in the monzodiorite as pockets of massive endoskarn. Mineralization of these features is characterized by molybdenite mineralization overprinting massive Ca and Mg exoskarns (Mo grade up to 0.30 wt. %), or magnetite overprinting massive Mg exoskarns (Fe grade up to 55 wt. %) with low Mo grade (typically 0.04 - 0.07 wt. % Mo). Chalcopyrite occurs in massive Mg and Ca exoskarns with molybdenite, however, nowhere in the Xiaojiayingzi mineral system does chalcopyrite reach economic concentration. Stratiform exoskarn mineralization occurs proximal to the granite porphyry, and is characterized by its extensive morphology (up to 1400 m in length; Fig. 5), and probably formed as a result of ore-forming fluids that travelled along highly permeable beds of the Wumishan Formation (e.g., Meinert et al., 2005). These features have variable magnetite and sulfides contents, with some rich in magnetite, whereas others have high molybdenite content. Finally, vein-type exoskarn mineralization commonly occurs in the intermediate and distal Ca exoskarns, where only part of the limestone is replaced by skarn minerals (Appendix Figure 3c-d). The vein-type exoskarn mineralization consists of garnet, pyroxene, and molybdenite with traces of chalcopyrite and pyrite, and is commonly narrow and elongated. Comparatively, this sub-type of exoskarn mineralization is of less economic importance than the massive and stratiform exoskarn mineralization in the Xiaojiayingzi mineral system.

Outside of the skarns, there is also minor carbonate-replacement Pb-Zn-Ag mineralization, which occurs as quartz - fluorite - galena - sphalerite - pyrite - bismuthinite ± chalcopyrite or quartz - fluorite ± galena ± sphalerite veins, developed in the Wumishan Formation. This type of mineralization does not contain any molybdenite, and is not described here in detail.

Zircon U-Pb geochronology

The U-Pb dating results are shown in Figure 12. Uncertainties are presented as ±x/y/z (analytical uncertainty/+tracer calibration/+decay constant uncertainty). The complete data sets are provided in Appendix Table S4. All results are represented with 2σ uncertainties. We use Th-corrected $^{206}Pb/^{238}U$ ages for all of our interpretations of the zircon geochronology because this chronometer provides the most precise and accurate estimate for rocks of this age range.

Nine zircon grains from the gabbroic diorite (CXJYZ) show a large spread of ages, ranging from 166.816 ± 0.064 to 164.701 ± 0.070 Ma. There are two grains which are distinctively older (166.816 ± 0.064, 166.230 ± 0.093 Ma), as well as one which is distinctly younger (164.701 ± 0.070 Ma). The remaining grains all overlap within uncertainty. This overlapping cluster of five zircons yielded a weighted mean age of 165.359 ± 0.028/0.052/0.18 Ma (MSWD=1.0). Nine zircons from the monzodiorite (QXJYZ) yielded ages spanning from 165.612 ± 0.273 to 165.306

± 0.119 Ma, with two outliers with ages of 166.739 ± 0.208 and 162.854 ± 0.162 Ma, respectively. The seven overlapping analyses from QXJYZ yielded a weighted mean $^{206}Pb/^{238}U$ age of 165.361 ± 0.040/0.059/0.19 Ma (MSWD=1.7). Ten zircons of the granite porphyry (ZK31-5) yielded a large spread in ages, from 166.293 ± 0.065 to 164.560 ± 0.065 Ma, with outliers at both older (166.293 ± 0.065 Ma) and younger (164.560 ± 0.065 Ma) ages. The five overlapping analyses yielded a weighted mean $^{206}Pb/^{238}U$ age of 165.099 ± 0.026/0.051/0.180 Ma (MSWD=1.8).

Molybdenite Re-Os geochronology

The Re-Os dating results are shown in Figure 13. Uncertainties are presented as ±x/y/z (analytical uncertainty/+tracer calibration/+decay constant uncertainty). The complete data sets are provided in Table 2. All results are represented with 2σ uncertainties.

Molybdenite from the quartz-molybdenite-pyrite ± chalcopyrite vein sample (X-8), which cuts the monzodiorite, yielded a Re-Os model age of 165.48 ± 0.09/0.69/0.85 Ma. Molybdenite in two exoskarn samples (X-1, XJYZ-3) and one iron ore sample (X-3) yielded overlapping Re-Os model ages of 165.43 ± 0.11/0.67/0.85, 165.41 ± 0.09/0.73/0.89, and 165.39 ± 0.29/0.95/1.08 Ma, respectively, which overlaps within uncertainty with the age obtained for the molybdenite from the vein sample (X-8). Molybdenite from the endoskarn vein sample (X-4) yielded a Re-Os model age of 165.19 ± 0.10/0.67/0.84. Molybdenite in one exoskarn sample (XJYZ-1) returned a Re-Os model age of 165.03 ± 0.13/0.67/0.85, which is younger than the exoskarn samples of X-1 and XKYZ-3. The Re-Os model age of molybdenite from a quartz-molybdenite-pyrite veinlet hosted in the granite porphyry with sericite selvage (X-6-2) is 163.73 ± 0.09/0.70/0.86 Ma. Similarly, a quartz-molybdenite-pyrite vein from the monzodiorite with sericite-chlorite selvage (X-9) yielded a molybdenite Re-Os model age of 163.11 ± 0.11/0.70/0.86 Ma.

Discussion

Age of intrusions spatially associated with the Xiaojiayingzi deposit

High-precision geochronology of intrusions associated with ore deposits increasingly yield protracted, complex age spectra, complicated by the variable presence of Pb-loss, antecrysts and xenocrysts (e.g., Tapster et al., 2016; Buret et al., 2017; Li et al., 2017; Gaynor et al., 2019a; Large et al., 2020, 2021; Rosera et al., 2021). Zircon data from intrusions spatially associated with the Xiaojiayingzi Mo deposit are another example of this phenomenon. All samples present a range in ages beyond the uncertainty of individual analyses (Fig. 12), and therefore the full age spectra do not necessarily relate to a single geological event such as the emplacement and solidification of intrusions at Xiaojiayingzi. Therefore, determining emplacement ages for these intrusions requires further interpretation.

Antecrysts and xenocrysts are commonly observed in high-precision data sets of intermediate to felsic magmatic rocks, and this has led some studies to interpret the youngest zircon in a complicated, high precision age spectra as reflecting crystallization of a magma or the age of a volcanic eruption (e.g., Schaltegger et al., 2009). However, in many highly altered or mineralizing systems, anomalously young ages are increasingly common in higher precision data sets, in many cases contradicting relative age relationships, and have been interpreted to be the result of incomplete mitigation of Pb-loss during chemical abrasion due to high temperature hydrothermal alteration (e.g., Ovtcharova et al., 2015; Gaynor et al., 2019a; Rosera et al., 2021). In this interpretation, the youngest plateau of ages is considered to reflect the final crystallization of a magma, whereas older ages reflect inheritance of xenocrystic or antecrystic material, and younger ages reflect Pb-loss. Due to the high temperature alteration observed throughout the Xiaojiayingzi Mo deposit and the presence of anomalously young zircon in the three age spectra, we interpret the youngest grains in each sample of the age spectra to reflect unmitigated Pb-loss. Therefore, we interpret a crystallization age of 165.361 ± 0.040/0.059/0.19 Ma for sample QCJYZ (n = 7, MSWD = 1.7), 165.359 ± 0.028/0.052/0.18 Ma for sample CXJYZ (n = 5, MSWD = 1.0), and 165.099 ± 0.026/0.051/0.18 Ma for sample ZK31-5 (n = 5, MSWD = 1.8). Based upon this interpretation, it is not possible to temporally distinguish between the gabbroic diorite from the monzodiorite, although the monzodiorite is younger than gabbroic diorite based on field observations. The granite porphyry was emplaced approximately 250 kyr after the two more mafic intrusive units. Relative to existing whole-rock K-Ar and zircon U-Pb geochronology (Fig. 14; Gao et al., 1979; Dai et al., 2009), these new ages provide much more precise and accurate timing of intrusive magmatism at Xiaojiayingzi. Due to the relatively limited nature of exploration and geochronology for the ore deposit, it is unlikely that these ages completely encapsulate the temporal history of magmatism within the Xiaojiayingzi system.

Superimposed, episodic hydrothermal pulses

Molybdenite mineralization in the Xiaojiayingzi deposit mainly occurs as exoskarn in the carbonate rocks of the Wumishan Formation, endoskarn in the monzodiorite, and molybdenite-bearing veins/veinlets in the monzodiorite and granite porphyry. The new molybdenite Re-Os geochronology suggests that there were episodic periods of mineralization over a period of approximately 2.4 Myrs, characterized by at least three pulses of Mo mineralization, one between 166-165 Ma, and then the two between 164-163 Ma (Fig. 13). Exoskarn molybdenite mineralization occurred over a period of 400 ± 20 ka (165.43 ± 0.11 - 165.03 ± 0.13 Ma). Endoskarn molybdenite mineralization occurred during at least one pulse of mineralization at 165.19 ± 0.10 Ma. Finally, vein molybdenite mineralization occurred in at least three discrete, non-overlapping pulses (165.48 ± 0.09 Ma; 163.73 ± 0.09 Ma; 163.11 ± 0.11 Ma). Combining these new detailed observations with high-precision molybdenite geochronology data indicates that the process of molybdenite mineralization at Xiaojiayingzi was more complicated than previously thought (e.g., Dai et al. 2009), and therefore requires evaluation and interpretation. These protracted dates could be the result of either preferential loss of radiogenic Os or overgrowth of younger molybdenite crystallization events during subsequent fluid alteration and mineralization events. However, the molybdenite Re-Os geochronology is robust to alteration (e.g., Stein et al., 2002), and none of the samples show evidence of secondary mineralization events in the form of temperature reversals in their alteration assemblage (Appendix Table S2), indicative of later high temperature events (e.g., Seedorff and Einaudi, 2004). Therefore, it is likely that mineralization of the Xiaojiayingzi system was the result of significantly protracted, superimposed, and episodic processes, and that these dates reflect unique periods of molybdenite mineralization. Although this Re-Os data set represents one of the most detailed high-precision geochronology studies of molybdenite skarn mineralization, it is likely that additional pulses of mineralization have not been recognized due to the lack of additional data or the resolution of the existing data, as the lifespans of individual hydrothermal systems are likely far lower than the duration of exoskarn formation (e.g., Cathles et al., 1997) and under-sampling may not reveal all mineralization.

Integrating magmatic and hydrothermal geochronology

Prior to the discovery of the Kangzhangzi ore block, exploration data from the Xiaojiayingzi ore block indicated that molybdenite mineralization mainly occurs as exoskarn in areas proximal to the monzodiorite, with relatively less molybdenite found in endoskarn and molybdenite-bearing quartz veins in the monzodiorite (Gao et al., 1979). For this reason, several researchers proposed a "new" class of Mo skarn deposit, the diorite-related Mo skarn deposit (e.g., Gao et al., 1979; Dai et al., 2009; Chen et al., 2017). This model significantly diverges from the generally accepted formational paradigm for other major Mo skarn deposits in the world, which are typically associated with fluids derived from felsic magmas (Meinert et al., 2005 and reference therein). Detailed field studies and high-precision geochronology of the Xiaojiayingzi deposit offers an excellent opportunity to test this model, by examining the potential genetic relationship between mafic intrusions and molybdenite mineralization.

Integrating field relationships with high-precision U-Pb zircon geochronology indicates that the Xiaojiayingzi intrusive complex was assembled through the progressive emplacement of the gabbroic diorite, monzodiorite, and granite porphyry intrusions over a period of approximately 250 kyr (Fig. 12). Furthermore, high-precision Re-Os molybdenite geochronology indicates that molybdenite mineralization was also episodic, with at least three different periods of mineralization based on the internal uncertainties of these data (Fig. 13). However, to directly compare the timing of intrusive crystallization to molybdenite mineralization, uncertainties in the decay constants, tracer calibrations, and analytical uncertainty for the two different isotopic systems must be taken into account. With these uncertainties, six of the eight molybdenite samples overlap within uncertainty with the U-Pb ages, whereas the remaining two samples are younger than any sampled intrusions (Fig. 14a). These new geochronology data indicate that molybdenite mineralization may have been coeval with monzodiorite magma emplacement, but that this period of mineralization was also coeval with granite porphyry emplacement, and there were two additional pulses of mineralization significantly afterward the solidification of the monzodiorite and granite porphyry intrusions (i.e., related to unexposed, deeper intrusions). These observations provide a direct challenge to models suggesting that Mo mineralization was only driven by mafic magmatism at the Xiaojiayingzi deposit. This conclusion is also consistent with field observations that both the monzodiorite and granite porphyry intrusions are spatially associated with skarns and associated Mo and Fe orebodies, and these skarns also have decreasing garnet/pyroxene abundances with increasing distance from these two intrusions (Figs. 3-4). This suggests that both monzodiorite and granite porphyry may have been the causative intrusions for the Mo skarn mineralization in the Xiaojiayingzi system. Additionally, molybdenite mineralization also occurred after the intrusion of the monzodiorite (e.g., sample X-9) and the granite porphyry (e.g., sample X-6-2), which suggests that there are other mineralizing intrusions associated with the Xiaojiayingzi deposit which are not exposed and have not been intercepted by exploratory drilling.

The detailed high-precision zircon U-Pb and molybdenite Re-Os geochronology presented in this study thus allows us to propose a new model for the formation of the Xiaojiayingzi Mo skarn deposit (Fig. 15). At ca. 165.36 Ma, mafic magmatism intruded and caused initial skarn formation, generating significant localized anisotropies and depositing Fe ore and potentially also Mo ore. Then at ca. 165.10 Ma, the intrusion of the granite porphyry is associated with another pulse of Mo and/or Fe mineralizing fluids based on field relationships (Figs. 4, 8c; Appendix Figure 2b), which subsequently mineralizes the surrounding wall rock, particularly exploiting the skarn anisotropies generated from the earlier emplacement. While it is possible that earlier, mafic magmatism did contribute Mo mineralization to the deposit, based on the above discussion we interpret that the granite porphyry is more likely to be responsible for economic mineralization. After approximately a million years, at ca. 164-163 Ma, the Xiaojiayingzi system received further metal enrichment from later mineralization events (i.e., unexposed mineralizing intrusions), which continued to overprint and enrich the ore grade at previously mineralized locations, and enhanced the vertical extent of mineralization.

Finally, by combining the mineralization and magmatic ages, it is possible to interpret a reason for anomalously young U-Pb zircon ages of the Xiaojiayingzi intrusive complex as shown in Figure 12. Molybdenite mineralization and associated fluid alteration episodically affected the three intrusive units between approximately 165-163 Ma. We interpret that these periods of fluid alteration may have affected some of the U-Pb systematics in the zircon from the Xiaojiayingzi deposit, and chemical abrasion was not able to completely mitigate the Pb-loss associated with these fluid alteration events. The degree to which Pb-loss will affect individual crystals likely varies between crystals as well. Therefore, we suggest that the interpreted weighted mean ages reflect an accurate crystallization age of the three intrusive units, because it is unlikely that multiple grains would experience identical Pb-loss necessary to give consistent, overlapping dates. Similar conclusions have been reached for zircon age spectra from other mineralizing or heavily altered rocks (e.g., Ovtcharova et al., 2015; Gaynor et al., 2019a; Rosera et al., 2020). Given that recent research has commonly interpreted the full range of high-precision zircon ages to reflect significant magmatic processes (e.g., Curry et al., 2021; Large et al., 2021; Schaen et al., 2021), we suggest caution when studying mineralized or highly altered rocks because it is possible to have unmitigated Pb-loss and therefore artificially protracted age spectra. Although the anomalously young grain from the monzodiorite aligns temporally with younger periods of molybdenite mineralization, it is not reasonable to take these younger ages as timing for younger periods of fluid alteration and mineralization because zircon alteration is not necessarily a complete resetting of its U-Pb systematics.

Implications for skarn deposit genesis and exploration

Skarn ore deposits are commonly characterized by two consecutive stages: an early prograde stage which forms anhydrous minerals (e.g., garnet, pyroxene) from relatively high-temperature, hypersaline fluid, and a later retrograde stage which precipitates hydrous minerals (e.g., epidote, amphibole, chlorite, sulfide ore minerals) from lower temperature, lower salinity fluids (Meinert et al., 2005). The difference between the two stages is commonly thought to reflect cooling of the magmatic-hydrothermal system after solidification of the associated magma (Meinert et al., 2003; Baker et al., 2004). However, few measurements exist on the timescale and duration of skarn mineralization, and therefore there is significant room for advancing our understanding of these systems. For example, where prograde alteration almost invariably predates retrograde alteration, it is unclear whether it is commonly a cyclical process, with episodic injections of new fluids.

The multi-pulsed mineralization process indicated by our Re-Os dates at Xiaojiayingzi suggests that the periodic mineralization process, as it has been observed in some porphyry systems (e.g., Chelle-Michou et al., 2015; Li et al., 2017; Gaynor et al., 2019a, b; Zhao et al., 2021), also operates for skarn deposits. Given the skarns at Xiaojiayingzi are fairly classical relative to other skarn deposits worldwide, the hypothesis proposed in this study could describe a fundamental process during the magmatic-hydrothermal evolution in skarn mineral systems. By inference, we suggest that the periodic magmatic-hydrothermal processes during skarn ore formation proposed here are common in skarn deposits and are linked with the episodic magmatic process occurring at depth within the source pluton. The significance of multi-pulsed magmatic-hydrothermal process is that each pulse can induce a similar metasomatism alteration pattern and enhance the economic resource in a geologically focused area. As such, this multi-pulsed alteration and mineralization of skarns at the Xiaojiayingzi deposit may be a necessary factor in forming large skarn deposits.

A cross-section across the Xiaojiayingzi and Kangzhangzi ore blocks shows molybdenite mineralization in the Xiaojiayingzi deposit changes from the steeply dipping monozodiorite related skarn- and porphyry-type mineralization at shallow levels (< 800 below the current ground surface) into the granite porphyry related skarn- and porphyry-types mineralization at depth (> 800 below the current ground surface; Fig. 4). Similar spatial relationships between the causative intrusions and skarn- and porphyry-types mineralization have also been observed in the Yerington batholith (a composite intrusive complex), Nevada, which hosts one Cu skarn deposit (i.e., Ludwig) at shallow levels and two coeval Cu porphyry (i.e., Ann-Mason and MacArthur) deposits at deeper levels (Harris and Einaudi, 1982; Dilles et al., 2000; Seedorff et al., 2008). As a result, identifying skarn deposits associated with multiphase intrusive systems may be a target for future exploration as it may point to previously undiscovered mineral resources.

Moreover, skarn formation ages are commonly interpreted from crystallization ages of assumed causative intrusive igneous bodies (e.g., Li et al., 2019) or crystallization ages of skarn garnet (e.g., Gevedon et al., 2018). These approaches are problematic, as causative intrusions may be either spatially removed or obfuscated by multiphase intrusive histories, and as metasomatism process (i.e., prograde and retrograde alterations) in large skarn deposits is cyclical, making links between igneous ages and skarn mineralization ambiguous. The two pulses of mineralization postdating intrusive assembly proximal to the skarns at Xiaojiayingzi indicate that the timing of mineralization cannot be simply inferred from dating local igneous rocks. Instead, where initial skarn formation may have been a rapid process directly associated with monzodiorite intrusion, skarn mineralization occurred over at least several million years. Directly dating mineralization is thus critical to yield a comprehensive understanding of the timescale of skarn ore formation, and it is crucial to use accurate, high-precision techniques in order to reveal the potential complex histories of these deposits.

Conclusions

Detailed evaluation of the Xiaojiayingzi Mo skarn mineral system through field relationships between intrusion phases, mineralization, and hydrothermal alteration, integrating these observations into a broader exploration data set, and new high-precision geochronology revealed a more complicated deposit assembly than previously recognized. Mineralization in the two ore blocks of the Xiaojiayingzi Mo skarn mineral system is spatially related to an intrusive complex, which is composed of gabbroic diorite, monzodiorite, and granite porphyry intrusions. In the Kangzhangzi ore block, skarn mineralization is zoned around the granite porphyry, whereas in the Xiaojiayingzi ore block, skarn mineralization is mostly developed in areas close to the contact between the monzodiorite and the Wumishan Formation. In both ore blocks, skarn mineralization converges downward into mineralized granite porphyry. In the Kangzhangzi ore block, skarns proximal to the granite porphyry have abundant garnets with compositions ranging from $Gro_{77}And_{21}$ to $Gro_{18}And_{75}$ and upwards to the Wumishan Formation are gradually dominated by pyroxene with compositions ranging from $Di_{22}Hd_{74}Jo_{5}$ to $Di_{4}Hd_{94}Jo_{3}$. In the Xiaojiayingzi ore block, garnets are abundant proximal to the monzodiorite and pyroxene increases away from the monzodiorite - Wumishan Formation contact. In agreement with the general skarn mineral zonation pattern, pyroxene becomes more Fe- and Mn-rich towards to the distal part of the skarn system, suggesting that skarn alteration and mineralization in the Xiaojiayingizi mineral system were associated with both of the monzodiorite and granite porphyry intrusions.

High-precision CA-ID-TIMS U-Pb zircon geochronology, coupled with cross-cutting relationships, indicates the gabbroic diorite crystallized at 165.359 ± 0.028/0.052/0.18 Ma, with subsequent crystallization of the monzodiorite and granite porphyry at 165.361 ± 0.040/0.059/0.19 Ma and 165.099 ± 0.026/0.051/0.18 Ma, respectively. High-precision Re-Os ages for molybdenite from the Xiaojiayingzi deposit distinguish at least three episodes of molybdenum mineralization (165.48 ± 0.09 - 165.03 ± 0.13, 163.73 ± 0.09, and 163.11 ± 0.11 Ma). Some of Re-Os ages for the mineralizing events overlap within uncertainty with high-precision U-Pb zircon ages of the monzodiorite and granite porphyry intrusions, confirming a genetic link between molybdenum mineralization and the two intrusions. However, several molybdenite Re-Os ages are significantly younger than any of the sampled intrusions, indicating that later fluid events mineralized and enriched the deposit. This indicates that there might be a deeper mineralizing system associated with the deposit, which has significant implications for future exploration work. Altogether, these results indicate that the Xiaojiayingzi skarn system was formed by the temporal and spatial superimposition of multi-pulsed magmatic-hydrothermal events.

Acknowledgments

This research was supported by Scientific Research Fund of the China Central Non-Commercial Institute (No. KK2203, KK2013, and K1707). We are grateful to Chris Ottley and Geoff Nowell for analytical support at Durham University. DS acknowledges the Total endowment fund and the Dida Scholarship of CUG Wuhan. Constructive comments from Larry Meinert, Zhaoshan Chang, Massimo Chiaradia, and an anonymous reviewer are greatly appreciated.

References

Baker, T., Achterberg, E.V., Ryan, C.G., and Lang J.R., 2004, Composition and evolution of ore fluids in a magmatic-hydrothermal skarn deposit: Geology, v. 32, p. 117-120.

Barboni, M., Schoene, B., 2014, Short eruption window revealed by absolute crystal growth rates in a granitic magma: Nature Geoscience, v. 7, p. 524-528.

Bowring, J.F., McLean, N.M., and Bowring, S.A., 2011, Engineering cyber infrastructure for U-Pb geochronology: Tripoli and U-Pb_Redux, Geochemistry, Geophysics, Geosystems, DOI:10.1029/2010GC003478.

Buret, Y., Wotzlaw, J.F., Roozen, S., Guillong, M., von Quadt, A., and Heinrich, C.A., 2017, Zircon petrochronological evidence for a plutonic-volcanic connection in porphyry copper deposits: Geology, v. 45, p. 623-626.

Chang, Z.S., Shu, Q.H., and Meinert, L.D., 2019, Skarn deposits of China: SEG Special Publications, no. 22, p. 189-234.

Cathles, L.M., Erendi, A.H.J., and Barrie, T.J.E.G., 1997, How long can a hydrothermal system be sustained by a single intrusive event? Economic Geology, v. 92, p. 766-771.

Chelle-Michou, C., Chiaradia, M., Seiby, D., Ovtcharova, M., and Spikings, R.A., 2015, High-resolution geochronology of the Coroccohuayco porphyry-skarn deposit, Peru: A rapid product of the Incaic orogeny: Economic Geology, v. 110, p. 423-443.

Chen, Y.J., Pirajno, F., Li, N., and Deng, X.H., 2017, Molybdenum deposits in China: Ore Geology Reviews, v. 81, p. 401-404.

Condon, D.J., Schoene, B., McLean, N.M., Bowring, S.A., and Parrish, R.R., 2015, Metrology and traceability of U-Pb isotope dilution geochronology (EARTHTIME Tracer Calibration Part I): Geochimica et Cosmochimica Acta, v. 164, 464-480.

Creaser, R.A., Papanastassiou, D.A., and Wasserburg, G.J., 1991, Negative thermal ion mass spectrometry of osmium, rhenium and iridium: Geochimica et Cosmochimica Acta, v. 55, p. 397-401.

Curry, A., Gaynor, S.P., Davies, J.H.F.L., Ovtcharova, M., Simpson, G., and Caricchi, L., 2021, Timescales and thermal evolution of large silicic magma reservoirs during an ignimbrite flare-up: perspectives from zircon. Contributions to Mineralogy and Petrology, https://doi.org/10.1007/s00410-021-01862-w.

Dai, J.Z., Mao, J.W., Zhao, C.S., Li, F.R., Wang, R.T., Xie, G.Q., and Yang, F.Q., 2008, High salinity fluid characteristic and evolution of Xiaojiayingzi Mo (Fe) deposit, Liaoning province: Acta Petrologica Sinica, v. 24, p. 2124-2131 (in Chinese with English abstract).

Dai, J.Z., Mao, J.W., Zhao, C.S., Xie, G.Q., Yang, F.Q., and Wang, Y.T., 2009, New U-Pb and Re-Os age data and the geodynamic setting of the Xiaojiayingzi Mo (Fe) deposit, western Liaoning province, Northeastern China: Ore Geology Reviews, v. 35, p. 235-244.

Dai, J.Z., Xie, G.Q., Wang, R.T., Ren, T., Wang, T., and Zhang, X.S., 2013, Metal sources of Xiaojiayingzi Mo (Fe) deposit: Evidence from PGE and S isotope analyses: Mineral Deposit, v. 32, p. 273-279 (in Chinese with English abstract).

Dilles, J.H., Einaudi, M.T., Proffett, J.M., and Barton, M.D., 2000, Overview of the Yerington porphyry copper district: Magmatic to nonmagmatic sources of hydrothermal fluids: Their flow paths and alteration effects on rocks and Cu-Mo-Fe-Au ores: Society of Economic Geologists Guidebook Series, v. 32, p. 55-66.

Eddy, M.P., Bowring, S.A., Miller, R.B., Tepper, J.H., 2016, Rapid assembly and crystallization of a fossil large-volume silicic magma chamber: Geology, v. 44, p. 331-334.

Feely, M., Costanzo, A., Gaynor, S. P., Selby, D., and McNulty, E., 2020, A review of molybdenite, and fluorite mineralization in Caledonian granite basement, western Ireland, incorporating new field and fluid inclusion studies, and Re-Os and U-Pb geochronology: Lithos, https://doi.org/10.1016/j.lithos.2019.105267.

Gao, Y.H., Kang, S.Z., Xiao, L.H., and Gao, G.L., 1979, The first prospecting report of the Xiaojiayingzi Mo deposit, Kazuo country, Liaoning province: 108 Geological Brigade, Liaoning Nonferrous Geological Bureau p. 136 (in Chinese).

Gaynor, S.P., Rosera, J.M., and Coleman, D.S., 2019a, Intrusive history of the Oligocene porphyry molybdenum deposit, New Mexico: Geosphere, v. 15, p. 548-575.

Gaynor, S.P., Coleman, D.S., Rosera, J.M., and Tappa, M.J., 2019b, Geochronology of a Bouguer gravity low: Journal of Geophysical Research: Solid Earth, v. 124, p. 2457-2468.

Gevedon, M., Seman, S., Barnes, J.D., Lachey, J.S., and Stockli, D.F., 2018, Unraveling histories of hydrothermal systems via U-Pb laser ablation dating of skarn garnet. Earth and Planetary Science Letters, v. 498: 237-246.

Guan, J.C., Ji, D.S., Long, J., Xu, P.F., Wei, Q., and Quan, W.L., 2010, Exploration report of the Kangzhangzi Mo-(Fe) deposit, Chaoxiang county, Liaoning province, 109 Geological Brigade, Liaoning Nonferrous Geological Bureau p. 74 (in Chinese).

Harris, N.B., and Einaudi, M.T., 1982, Skarn deposits in the Yerington District, Nevada; metasomatic skarn evolution near Ludwig: Economic Geology, v. 77, p. 877-898.

Hiess, J., Condon, D.J., McLean, N., and Noble, S.R., 2012, $^{238}U/^{235}U$ systematics in terrestrial uranium-bearing minerals: Science, v., 335, p. 1610-1614.

Krogh, T. E., 1973, A low-contamination method for hydrothermal decomposition of zircon and extraction of U and Pb for isotopic age determinations: Geochimica et Cosmochimica Acta, v. 37, p. 485-494.

Large, S.J., Wotzlaw, J.F., Guillong, M., Quadt, A.V., and Heinrich, C.A. 2020, Resolving the timescales of magmatic and hydrothermal processes associated with porphyry deposit formation using zircon U-Pb petrochronology: Geochronology, v. 2, p. 209-230.

Large, S.J.E., Buret, Y., Wotzlaw, J.F., Karakas, O., Guillong, M., von Quadt, A., and Heinrich, C.A., 2021, Copper-mineralised porphyries sample the evolution of a large-volume silicic magma reservoir from rapid assembly to solidification: Earth and Planetary Science Letters, doi.org/10.1016/j.epsl.2021.116877.

Lawley, C.J.M., and Selby, D., 2012, Re-Os geochronology of quartz-enclosed ultrafine molybdenite: Implications for ore geochronology: Economic Geology, v. 107, p. 1499-1505.

Leuthold, J., Müntener, O., Baumgartner, L.P., Putlitz, B., Ovtcharova, M., Schaltegger, U., 2012, Time resolved construction of a bimodal laccolith (Torres del Paine, Patagonia): Earth and Planetary Science Letters, v. 325-326, p. 85-92.

Li, J. W., Bi, S. J., Selby, D., Chen, L., Vasconcelos, P., Thiede, D., Zhou, M. F., Zhao, X. F., Li, Z. K., and Qiu, H. N., 2012, Giant Mesozoic gold provinces related to the destruction of the North China craton: Earth and Planetary Science Letters, v. 349, p. 26-37.

Li, W., Xie, G.Q., Mao, J.W., Zhu, Q.Q., and Zheng, J.H., 2019, Mineralogy, fluid inclusion, and stable isotope studies of the Chengchao deposit, Hubei province, eastern China: Implications for the formation of high-grade Fe skarn deposits: Economic Geology, v. 114, p. 325-352.

Li, Y., Selby, D., Condon, D., and Tapster, S., 2017, Cyclic magmatic-hydrothermal evolution in porphyry systems: high-precision U-Pb and Re-Os geochronology constraints on the Tibetan Qulong porphyry Cu-Mo deposit: Economic Geology, v. 112, p. 1419-1440.

Liu, J.L., Davis, G.A., Lin, Z.Y., and Wu, F.Y., 2005, The Liaonan metamorphic core complex, Southeastern Liaoning Province, North China: A likely contributor to Cretaceous rotation of Eastern Liaoning, Korea and contiguous areas: Tectonophysics, v. 407, p. 65-80.

Liu, C.C., Yang, Z.J., Wang, C.L., Jiang, C.Y., and Yao, Z.H., 2012, Metallogenic model and prospecting model in Xiaojiayingzi molybdenum polymetallic deposit of Liaoning: Global Geology, v. 31, p. 238-246 (in Chinese with English abstract).

Ma, Q., Zheng, J.P., Griffin, W.L., Zhang, M., Tang, H.Y., Su, Y.P., and Ping, X.Q., 2012, Triassic "adakitic" rocks in an extensional setting (North China): melts from the cratonic lower crust: Lithos, v. 149, p. 159-173.

Mao, J.W., Ouyang, H.G., Song, S.W., Santosh, M., Yuan, S.D., Zhou, Z.H., Zheng, W., Liu, H., Liu, P., Cheng, Y.B., and Chen, M.H., 2019, Geology and metallogeny of tungsten and tin deposits in China, in Chang, Z., and Goldfarb, R.J., eds., Mineral Deposits of China: Society of Economic Geologists Special Publication, v. 22, p. 411-482.

Mao, J.W., Zheng, W., Xie, G.Q., Goldfarb, R.J., and Lehmann, B., 2021. Recognition of a Mid-Late Jurassic arc–related porphyry copper belt along the Southeast China coast: Geological characteristics and tectonic implications: Geology, v. 49, p. 592-596.

Mattinson, J.M., 2005, Zircon U-Pb chemical abrasion ("CA-TIMS") method: combined annealing and multi-step partial dissolution analysis for improved precision and accuracy of zircon ages: Chemical Geology, v. 220, p. 47-66.

McLean, N.M., Bowring, J.F., and Bowring, S.A., 2011, An algorithm for U-Pb isotope dilution data reduction and uncertainty propagation. Geochemistry, Geophysics, Geosystems, DOI:10.1029/2010GC003479.

Meinert, L.D., 1997, Application of skarn deposit zonation models to mineral exploration: Exploration and Mining Geology, v. 6, p. 185-208.

Meinert, L.D., Hederquist, J.W., Satoh, H., and Matsuhisa, Y., 2003, Formation of anhydrous and hydrous skarn in Cu-Au ore deposits by magmatic fluids, Economic Geology, v. 98, 147-156.

Meinert, L.D., Dipple, G.M., and Nicolescu, S., 2005, World skarn deposits: Economic Geology, v. 100th Anniversary Volume, p. 299-336.

Menzies, M.A., and Xu, Y.G., 1998, Geodynamics of the North China craton: Mantle dynamics and plate interactions in East Asia, v. 27, p. 155-165.

Mundil, R., Ludwig, K.R., Metcalf, I., and Renne, P.R., 2004, Age and timing of the Permian mass extinctions: U/Pb dating of closed-system zircons: Science, v. 305, p. 669-673.

Ouyang, H.G., Mao, J.W., Santosh, M., Zhou, J., Zhou, Z.H., Wu, Y., and Hou, L., 2013, Geodynamic setting of Mesozoic magmatism in NE China and surrounding regions: perspectives from spatio-temporal distribution patterns of ore deposits: Journal of Asian Earth Sciences, v. 78, p. 222-236.

Ouyang, H.G., Mao, J.W., and Hu, R.Z., 2020, Geochemistry and crystallization conditions of magmas related to porphyry Mo mineralization in northeastern China: Economic Geology, v. 115, p. 79-100.

Ovtcharova, M., Goudemand, N., Hammer, Ø., Guodun, K., Cordey, F., Galfetti, T., Schaltegger, U., and Bucher, H., 2015, Developing a strategy for accurate definition of a geological boundary through radio-isotopic and biochronological dating: The Early–Middle Triassic boundary (South China): Earth-Science Reviews, v. 146, p. 65-76.

Ren, J.Y., Tamaki, K., Li, S.T., and Zhang, J.X., 2002, Late Mesozoic and Cenozoic rifting and its dynamic setting in Eastern China and adjacent areas: Tectonophysics, v. 344, p. 175-205.

Rosera, J.M., Coleman, D.S., and Stein, H.J., 2013, Re-evaluating genetic models for porphyry Mo mineralization at Questa, New Mexico: Implications for ore deposition following silicic ignimbrite eruption: Geochemistry, Geophysics, Geosystems, v. 14, p. 787-805.

Rosera, J.M., Gaynor, S.P., Coleman, D.S., 2021, Spatio-temporal shifts in magmatism and mineralization in northern Colorado beginning in the late Eocene: Economic Geology, v. 116, p. 987-1010.

Schaen, A.J., Schoene, B., Dufek, J., Singer, B.S., Eddy, M.P., Jicha, B.R., and Cottle, J.M., 2021, Transient rhyolite melt extraction to produce a shallow granitic pluton. Science Advances, DOI: 10.1126/sciadv.abf0604.

Schaltegger, U., Brack, P., Ovtcharova, M., Peytcheva, I., Schoene, B., Stracke, A., Marocchi, M., Bargossi, G.M., 2009, Zircon and titanite recording 1.5 million years of magma accretion, crystallization and initial cooling in a composite pluton (southern Adamello batholith, northern Italy): Earth and Planetary Science Letters, v. 286, p. 208-218.

Schaltegger, U., Ovtcharova, M., Gaynor, S. P., Schoene, B., Wotlzaw, J.F., Davies, J.H.F.L., Farina, F., Greber, N., Szymanowski, D., and Chelle-Michou, C., 2021, Long-term repeatability and interlaboratory reproducibility of high-precision ID-TIMS U-Pb geochronology: Journal of Analytical Atomic Spectrometry. DOI: 10.1039/d1ja00116g.

Seedorff, E., and Einaudi, M.T., 2004, Henderson porphyry molybdenum system, Colorado: I. Sequence and abundance of hydrothermal mineral assemblages, flow paths of evolving fluids, and evolutionary style. Economic Geology, v. 99, p. 3-37.

Seedorff, E., Barton, M.D., Stavast, W.J., and Maher, D.J., 2008, Root zones of porphyry systems: Extending the porphyry model to depth: Economic Geology, v. 103, p. 939-956.

Selby, D., and Creaser, R.A., 2001, Re-Os geochronology and systematics in molybdenite from the Endako porphyry molybdenum deposit, British Columbia, Canada: Economic Geology, v. 96, p. 197-204.

Smoliar, M.I., Walker, R.J., and Morgan, J.W., 1996, Re-Os ages of group IIA, IIIA, IVA, and IVB iron meteorites: Science, v. 271, p. 1099-1102.

Stein, H.J., Markey, R.J., Morgan, J.W., Hannah, J.L., and Scherstén, A., 2001. The remarkable

Re-Os chronometer in molybdenite: how and why it works. Terra Nova, v. 13, p. 479-486.

Shu, Q.H., Chang, Z.S., Lai, Y., Zhou, Y.T., Sun, Y., and Yan, C., 2016, Regional metallogeny of Mo-bearing deposits in northeastern China, with new Re-Os dates of porphyry Mo deposits in the northern Xilamulun district: Economic Geology, v. 111, p. 1783-1798.

Sun, W.D., Ding, X., Hu, Y.H., and Li, X.H., 2007, The golden transformation of the Cretaceous plate subduction in the west Pacific: Earth and Planetary Science Letters, v. 262, p. 533-542.

Tapster, S., Condon, D.J., Naden, J., Noble, S.R., Petterson, M.G., Roberts, N.M.W., Saunders, A.D., and Smith, D.J., 2016, Rapid thermal rejuvenation of high-crystallinity magma linked to porphyry copper deposit formation; evidence from the Koloua Porphyry Prospect, Solomon Islands: Earth and Planetary Science Letters, v. 442, p. 206-217.

Widmann, P., Davies, J.H.F.L., and Schaltegger, U., 2019, Calibrating chemical abrasion: Its effects on zircon crystal structure, chemical composition and U-Pb age: Chemical Geology, v. 511, p. 1-10.

Wu, F.Y., Yang, J.H., Zhang, Y.B., and Liu, X.M., 2006, Emplacement ages of the Mesozoic granites in southeastern part of the Western Liaoning province: Acta Petrologica Sinica, v. 22, p. 315-325.

Xiao, W.J., Windley, B.F., Hao, J., and Zhai, M.G., 2003, Accretion leading to collision and the Permian Solonker suture, Inner Mongolia, China: termination of the central Asian orogenic belt: Tectonics, doi.10.1029/2002TC001484.

Yang, J.H., Wu, F.Y., Wilde, S.A., and Liu, X.M., 2007, Petrogenesis of Late Triassic granitoids and their enclaves with implications for post-collisional lithospheric thinning of the Liaodong Peninsula, North China Craton: Chemical Geology, v. 242, p. 155-175.

Yang, W., and Li, S.G., 2008, Geochronology and geochemistry of the Mesozoic volcanic rocks in Western Liaoning: Implications for lithospheric thinning of the North China Craton: Lithos, v. 102, p. 88-117.

Yang, Z.Y., Cheng, Y.Q., and Wang, H.Z., 1986, The geology of China: New York, Oxford University Press, 306 p.

Yu, Z.X., Ao, Y.F., Lv, J.Z., Long, J., Jia, G.N., Wang, H.F., and Zhang, L., 2009, The application of CSAMT in prospecting in dept in Kangjzhangzi deposit in western Liaoning province: Geology and Exploration, v. 45, p. 600-605 (in Chinese with English abstract).

Yu, Z.X., Long, J., Li, C.L., Ji, D.S., Lv, J.F., and Huo, Z.H., 2014, Application of 3Dmine software in the digital resource information management in the Kangzhangzi Mo deposit area, western Liaoning Province: Mineral Exploration, v. 5, p. 58-62 (in Chinese with English abstract).

Zeng, Q.D., Liu, J.M., Qin, K.Z., Fan, H.R., Chu, S.X., Wang, Y.B., and Zhou, L.L., 2013, Types, characteristics, and time-space distribution of molybdenum deposits in China: International Geology Review, v. 55, p. 1311-1358.

Zhang, S.H., Zhao, Y., Davis, G.A., Ye, H., and Wu, F., 2014, Temporal and spatial variations of Mesozoic magmatism and deformation in the North China Craton: Implications for lithospheric thinning and decratonization: Earth-Science Reviews, v. 131, p. 49-87.

Zhao, Y.M., Lin, W.W., Bi, C.S., Li, D.X., and Jiang, C.J., 1990, Skarn deposits of China: Beijing, Geological Press, 354 p. (in Chinese).

Zhao, G.C., Wilde, S.A., Cawood, P.A., and Sun, M., 2001, Archean blocks and their boundaries in the North China Craton: lithological, geochemical, structural and P-T path constraints and tectonic evolution: Precambrian Research, v. 107, p. 45-73.

Zhao, Q.Q., Zhai, D.G., Mathur, R., Liu, J.J., Selby, D., and Williams-Jones, A.E., 2021, The giant Chalukou porphyry Mo deposit, northeast China: The product of a short-lived, high flux mineralization event: Economic Geology, v. 116, p. 1209-1225.

Zhu, R.X., Chen, L., Wu, F.Y., and Liu, J.L., 2011, Timing, scale and mechanism of the destruction of the North China Craton: Science China Earth Sciences, v. 54, p. 789-797.

Zimmerman, A., Stein, H.J., Morgan, J.W., Markey, R.J., and Watanabe, Y., 2014, Re-Os geochronology of the El Salvador porphyry Cu-Mo deposit, Chile: Tracking analytical improvements in accuracy and precision over the past decade: Geochimica et Cosmochimica Acta, v. 131, p. 13-32.

Figure captions

Fig. 1. (a) Simplified geological map of eastern China showing major tectonic units (modified from Yang et al., 2007). (b) Geological map showing the distribution of Mesozoic magmatism and mineral deposits in western Liaoning and location of the Xiaojiayingzi Mo deposit (modified from Wu et al., 2006).

Fig. 2. (a) Regional geological map of the Xiaojiayingzi district in western Liaoning (Yu et al., 2014). (d) Geological map of the Xiaojiayingzi Mo deposit (Yu et al., 2009). Cross-section locations of A-B, C-D, and E-F are also shown.

Fig. 3. Geological cross-section of the Xiaojiayingzi deposit, showing the spatial distribution of alteration and mineralization in the Xiaojiayingzi (a; modified from Gao et al., 1979) and Kangzhangzi (b; modified from Guan et al., 2010) ore blocks.

Fig. 4. Geological cross-section of the Xiaojiayingzi deposit, showing the spatial distribution of alteration and mineralization across the Xiaojiayingzi and Kangzhangzi ore blocks (modified from Guan et al., 2010).

Fig. 5. Photographs and photomicrographs of the three intrusions (i.e., gabbroic diorite, monzodiorite, and granite porphyry) of the Xiaojiayingzi intrusive complex. (a-b) Crosscutting relationships of the gabbroic diorite, monzodiorite, and granite porphyry. (c-d) Photograph and photomicrograph of the gabbroic diorite. (e-f) Photograph and photomicrograph of the monzodiorite. (g-h) Photograph and photomicrograph of the granite porphyry. Photomicrographs all under plane-polarized transmitted light. Afs = K-feldspar, Bt = biotite, Aug = augite, Hbl = hornblende, Pl = plagioclase, Qtz = quartz.

Fig. 6. Representative photographs and photomicrographs of mineralization and alteration in the gabbroic diorite. (a) Gabbroic diorite cut by quartz veinlets with K-feldspar envelopes and by quartz - pyrite veinlets with sericite - chlorite envelopes. (b) Plagioclase in gabbroic diorite partly

replaced by sericite (under plane-polarized transmitted light). (c-d) Molybdenite and chalcopyrite in altered gabbroic diorite (back-scattered electron images). Act = actinolite, Afs = K-feldspar, Aug = augite, Bn = bornite, Bt = biotite, Cal = calcite, Fl = fluorite, Hbl = hornblende, Phl = phlogopite, Pl = plagioclase, Px = pyroxene, Qtz = quartz, Ser = sericite, Mo = molybdenite, Mt = magnetite, Apt = apatite, Py = pyrite, Ccp = chalcopyrite, Gn = galena, Grt = garnet, Ilm = ilmenite, and Sp = sphalerite.

Fig. 7. Representative photographs and photomicrographs of mineralization and alteration in the monzodiorite. (a) Monzodiorite overprinted by sodic alteration, in turn was crosscut by endoskarn vein/veinlet with molybdenite mineralization. (b) Monzodiorite cut by quartz - molybdenite - pyrite vein with K-feldspar alteration envelopes. (c) Monzodiorite cut by quartz - molybdenite - pyrite - chalcopyrite - galena - sphalerite vein. (d) Enlarged region of Figure 7c, showing plagioclase in monzodiorite partly replaced by sericite with disseminated pyrite (under plane-polarized transmitted light). (e) Photomicrograph of the quartz - molybdenite - pyrite - chalcopyrite - galena- sphalerite vein in monzodiorite (under reflected light). (f) Breccias of silicified monzodiorite cemented by medium- to fine-grained molybdenite and pyrite, in turn overprinted by coarse-grained pyrite, fluorite, and quartz. Abbreviations as in Fig. 6.

Fig. 8. Representative photographs and photomicrographs of mineralization and alteration in the granite porphyry. (a) Granite porphyry cut by quartz veinlets. (b) Granite porphyry cut by quartz-biotite veinlets, in turn truncated by quartz-molybdenite veinlts with K-feldspar alteration halos. (c) Photomicrographs of (b) showing the quartz-biotite veinlets (under plane-polarized transmitted light). (d) Granite porphyry cut by quartz - molybdenite - pyrite and quartz - pyrite veins and veinlets with sericitic alteration halos. (e) Granite porphyry cut by quartz - molybdenite veinlets, in turn truncated by quartz veinlet. (f-g) Molybdenite, chalcopyrite, and bornite replace the groundmass of the granite porphyry along the grain boundary of the alkaline feldspar phenocrystal. They are of the same field of view with 8f under plane-polarized transmitted light and 8g under reflected light. (h) Granite porphyry with pervasive K-feldspar alteration cut by quartz - molybdenite - pyrite veinlets, in turn truncated by quartz - pyrite veins. Abbreviations as in Fig. 6.

Fig. 9. (a-b) Photograph and photomicrograph of the massive magnetite ore from the proximal skarn zone of the Xiaojiayingzi system, showing it consists of magnetite, phlogopite, pyroxene, and actinolite (b under plane-polarized transmitted light). (c) Massive magnetite ore overprinted by chalcopyrite and calcite. (d) Photomicrograph of (c), showing magnetite is earlier than molybdenite, chalcopyrite, galena, and calcite (under reflect light). (e) Massive magnetite ore overprinted by molybdenite, chalcopyrite, and calcite. (f) Garnet-bearing massive magnetite ore overprinted by chalcopyrite, molybdenite, and calcite. Abbreviations as in Fig. 6.

Fig. 10 (a) Massive Ca exoskarn from the proximal skarn zone of the Xiaojiayingzi system, showing garnet overprinted by retrograde mineral of actinolite and molybdenite. (b) Photomicrographs of (a) showing molybdenite occur along the grain boundaries of garnet (under reflected light). (c-d) Massive Ca exoskarn pervasively overprinted by retrograde minerals of actinolite, molybdenite, and chalcopyrite (d under reflected light). (e-f) Massive Ca exoskarn overprinted by molybdenite and calcite, in turn truncated by quartz veinlet (f under reflected light). Abbreviations as in Fig. 6.

Fig. 11. Ternary plots of the Xiaojiayingzi skarn garnet (a) and pyroxene (b) compositions. End members: And = andradite, Alm = almandine, Di = diopside, Hd = hedenbergite, Gro = grossularite, Jo = johannsenite, Spe = spessartine

Fig. 12. $^{206}Pb/^{238}U$ ages for individual zircon analyses from the Xiaojiayingzi Mo skarn deposit. Vertical bar height is the 2σ uncertainty of individual analyses. Data are plotted with internal uncertainties only; decay constant uncertainties are only needed with comparing to other geochronometers (e.g., Re-Os). Weighted mean 2σ uncertainties are reported as: internal only/internal with tracer calibration/internal, tracer calibration and with ^{238}U decay constant. Grains not included in weighted mean calculations are grayed out. See text for discussion.

Fig. 13. Molybdenite Re-Os geochronology from various ore samples from the Xiaojiayingzi Mo skarn deposit. Vertical bar height is the 2σ uncertainty of individual analyses. Data are plotted with internal uncertainties only; decay constant uncertainties are only needed with comparing to other

geochronometers (e.g., U-Pb). Vein molybdenite mineralization occurred in three geochronologically distinct periods, with Mo skarn mineralization occurring over a period of 400 ± 20 ka. See text for further discussion.

Fig. 14. Compilation of high-precision U-Pb and Re-Os data for the Xiaojiayingzi Mo skarn deposit. Vertical bar height is the 2σ uncertainty of individual analyses. Data are plotted with uncertainties in the decay constants, tracer calibrations, and analytical uncertainties. See text for further discussion. Previous SHRIMP zircon U-Pb and ID-ICP-MS molybdenite Re-Os data of Dai et al. (2009) are also shown for comparison.

Fig. 15. Cartoon shows the genetic model of the Xiaojiayingzi skarn Mo deposit. (a) At ca. 165.36 Ma, intrusion of monzodiorite into marble forms early skarn Fe and potentially also Mo mineralization. (b) At ca. 165.10 Ma, newly formed skarn and Mo and/or Fe mineralization associated with granite porphyry coalesce with earlier formed skarn and mineralization. Porphyry-style Mo mineralization associated with granite porphyry cut across monzodiorite; (c) At ca. 164-163 Ma, porphyry-style Mo mineralization associated with unexposed intrusions cut across monzodiorite and granite porphyry. In b and c, later skarn- and/or porphyry-style mineralization added to earlier skarns and intrusions, thereby enhanced the vertical extent of mineralization and possibly the ore grade as well.

Figure 1

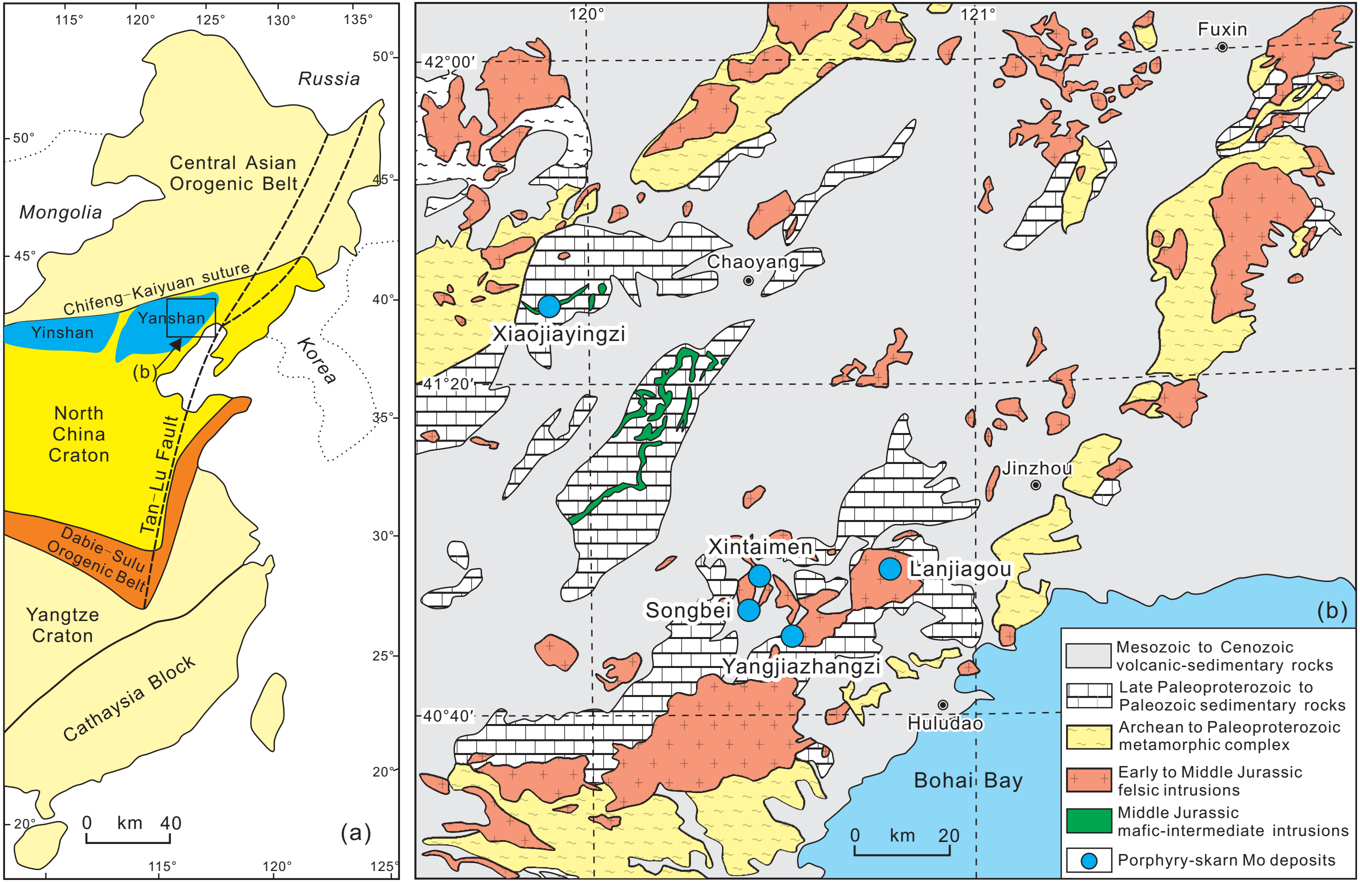

Russia
Mongolia
Central Asian Orogenic Belt
Chifeng–Kaiyuan suture
Yinshan
Yanshan
(b)
Korea
North China Craton
Tan-Lu Fault
Dabie–Sulu Orogenic Belt
Yangtze Craton
Cathaysia Block
0 km 40
(a)
Fuxin
Chaoyang
Xiaojiayingzi
Jinzhou
Xintaimen
Lanjiagou
Songbei
Yangjiazhangzi
Huludao
Bohai Bay
0 km 20
(b)
Mesozoic to Cenozoic volcanic-sedimentary rocks
Late Paleoproterozoic to Paleozoic sedimentary rocks
Archean to Paleoproterozoic metamorphic complex
Early to Middle Jurassic felsic intrusions
Middle Jurassic mafic-intermediate intrusions
Porphyry-skarn Mo deposits

Figure 2

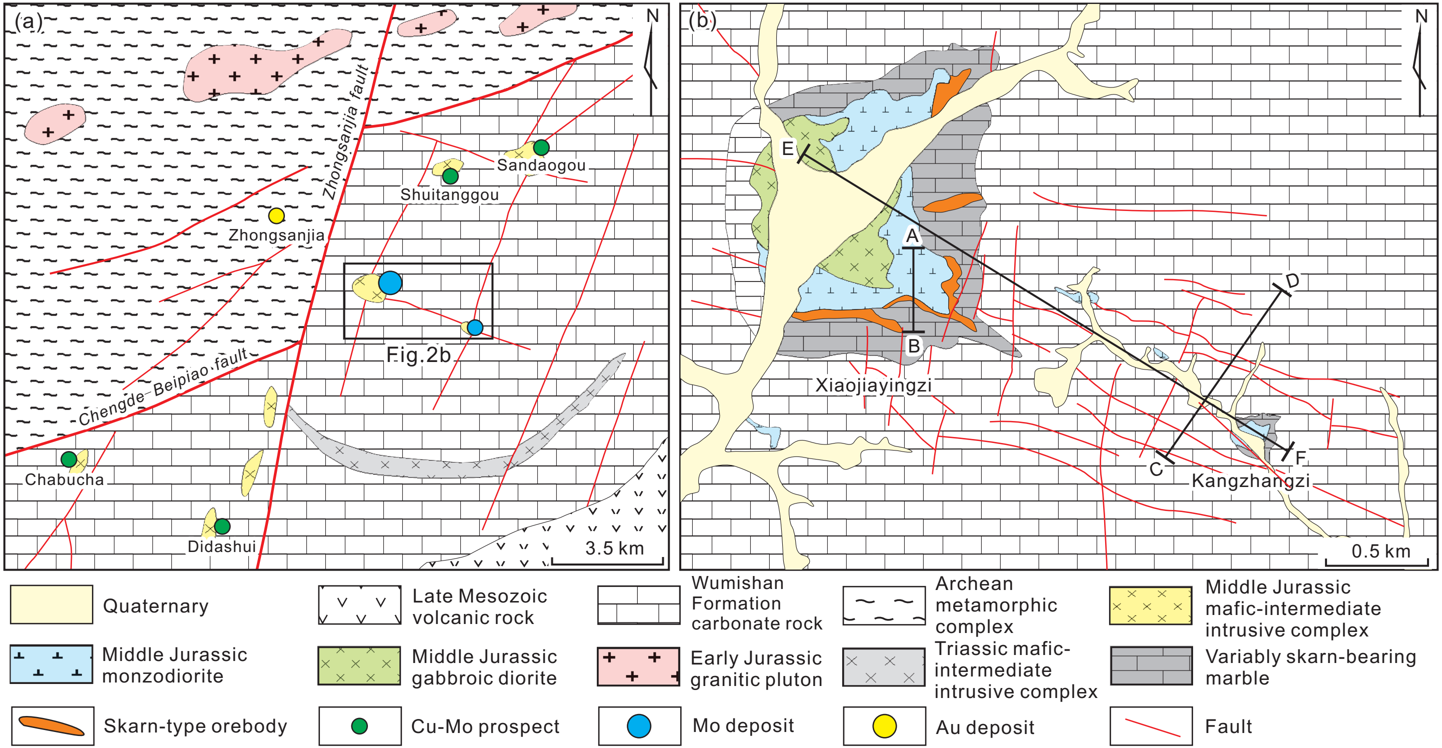
(a)
N
Zhongsanjia fault
Chengde–Beipiao fault
Sandaogou
Shuitanggou
Zhongsanjia
Fig.2b
Chabucha
Didashui
3.5 km
(b)
N
E
A
B
D
C
F
Xiaojiayingzi
Kangzhangzi
0.5 km
Quaternary
Late Mesozoic volcanic rock
Wumishan Formation carbonate rock
Archean metamorphic complex
Middle Jurassic mafic-intermediate intrusive complex
Middle Jurassic monzodiorite
Middle Jurassic gabbroic diorite
Early Jurassic granitic pluton
Triassic mafic-intermediate intrusive complex
Variably skarn-bearing marble
Skarn-type orebody
Cu-Mo prospect
Mo deposit
Au deposit
Fault

Figure 3

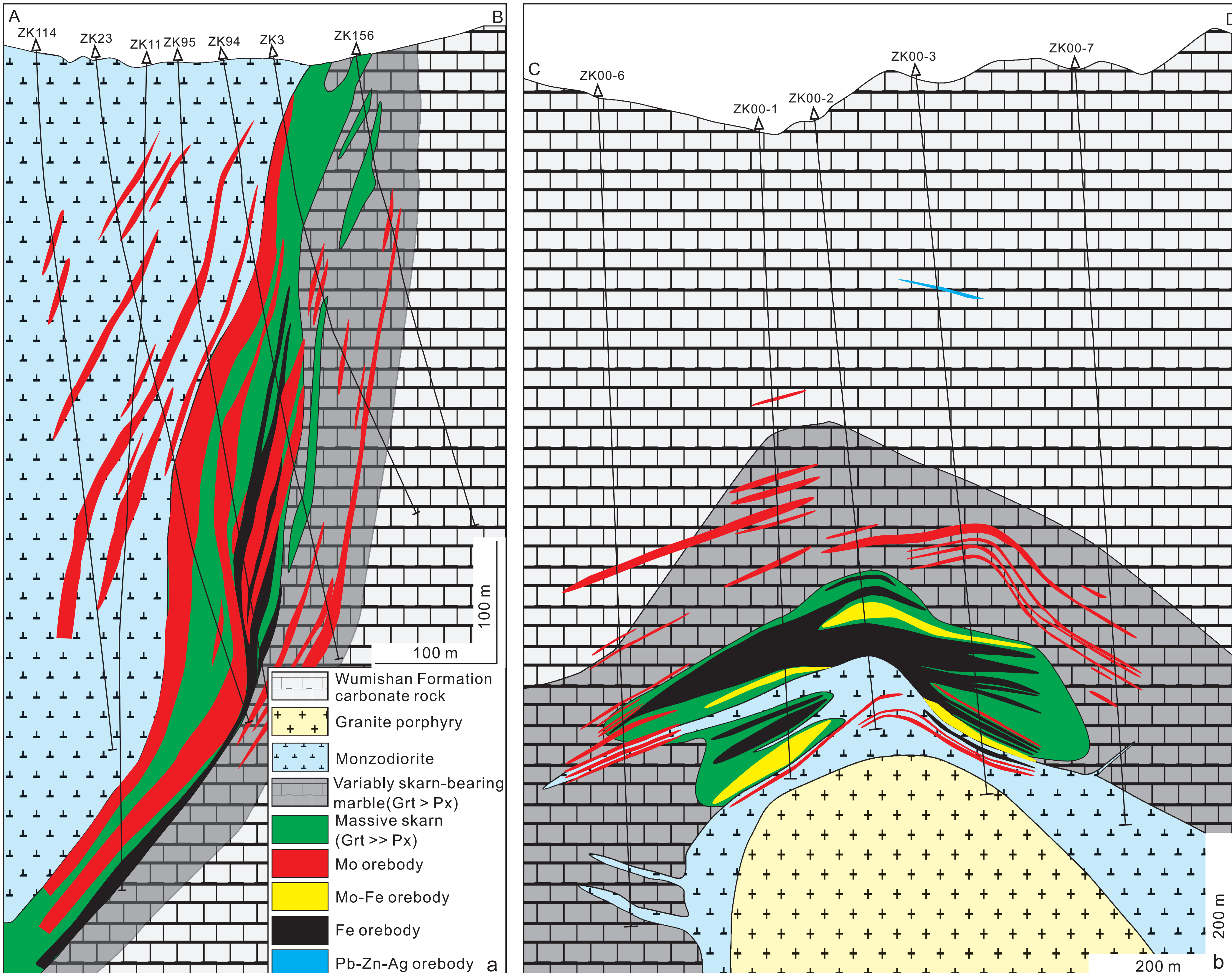

A
B
ZK114
ZK23
ZK11
ZK95
ZK94
ZK3
ZK156
100 m
100 m
C
D
ZK00-6
ZK00-1
ZK00-2
ZK00-3
ZK00-7
200 m
200 m
Wumishan Formation carbonate rock
Granite porphyry
Monzodiorite
Variably skarn-bearing marble(Grt > Px)
Massive skarn (Grt >> Px)
Mo orebody
Mo-Fe orebody
Fe orebody
Pb-Zn-Ag orebody
a
b

Figure 4

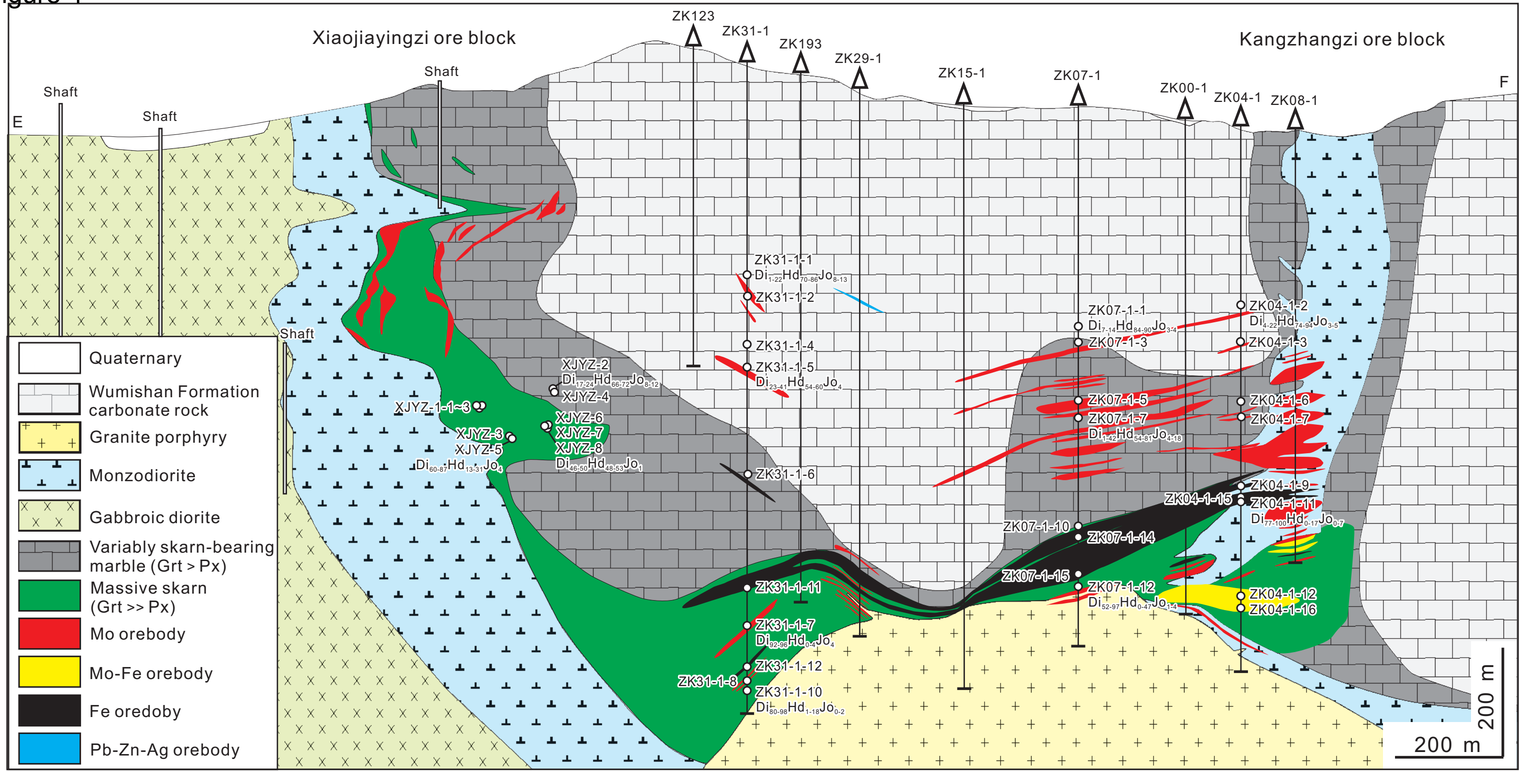

Xiaojiayingzi ore block
Kangzhangzi ore block
E
F
Shaft
Shaft
Shaft
Shaft
ZK123
ZK31-1
ZK193
ZK29-1
ZK15-1
ZK07-1
ZK00-1
ZK04-1
ZK08-1
ZK31-1-1
Di1-22Hd70-86Jo8-13
ZK31-1-2
ZK31-1-4
ZK31-1-5
Di23-41Hd54-60Jo4
ZK31-1-6
ZK31-1-11
ZK31-1-7
Di92-96Hd0-4Jo4
ZK31-1-12
ZK31-1-8
ZK31-1-10
Di80-98Hd1-18Jo0-2
XJYZ-2
Di17-24Hd66-72Jo8-12
XJYZ-4
XJYZ-1-1~3
XJYZ-6
XJYZ-7
XJYZ-8
Di46-50Hd48-53Jo1
XJYZ-3
XJYZ-5
Di60-87Hd13-31Jo4
ZK07-1-1
Di7-14Hd84-90Jo3-4
ZK07-1-3
ZK07-1-5
ZK07-1-7
Di1-42Hd54-81Jo4-18
ZK07-1-10
ZK07-1-14
ZK07-1-15
ZK07-1-12
Di52-97Hd0-47Jo1-4
ZK04-1-2
Di4-22Hd74-94Jo3-5
ZK04-1-3
ZK04-1-6
ZK04-1-7
ZK04-1-9
ZK04-1-15
ZK04-1-11
Di77-100Hd0-17Jo0-7
ZK04-1-12
ZK04-1-16
200 m
200 m
Quaternary
Wumishan Formation carbonate rock
Granite porphyry
Monzodiorite
Gabbroic diorite
Variably skarn-bearing marble (Grt > Px)
Massive skarn (Grt >> Px)
Mo orebody
Mo-Fe orebody
Fe oredoby
Pb-Zn-Ag orebody

Figure 5

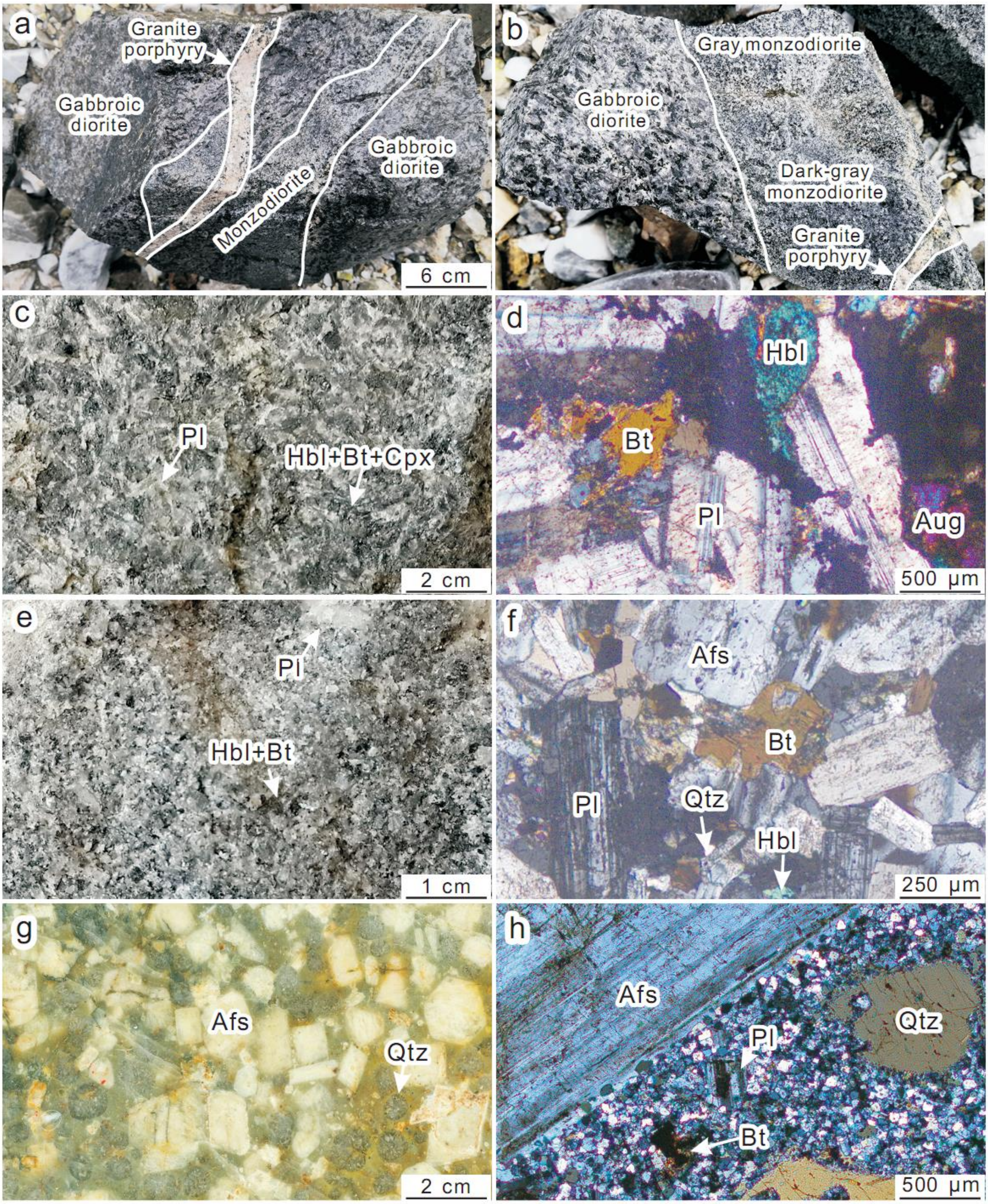
a
Granite porphyry
Gabbroic diorite
Monzodiorite
Gabbroic diorite
6 cm
b
Gray monzodiorite
Gabbroic diorite
Dark-gray monzodiorite
Granite porphyry
c
Pl
Hbl+Bt+Cpx
2 cm
d
Hbl
Bt
Pl
Aug
500 μm
e
Pl
Hbl+Bt
1 cm
f
Afs
Bt
Pl
Qtz
Hbl
250 μm
g
Afs
Qtz
2 cm
h
Afs
Qtz
Pl
Bt
500 μm

Figure 6

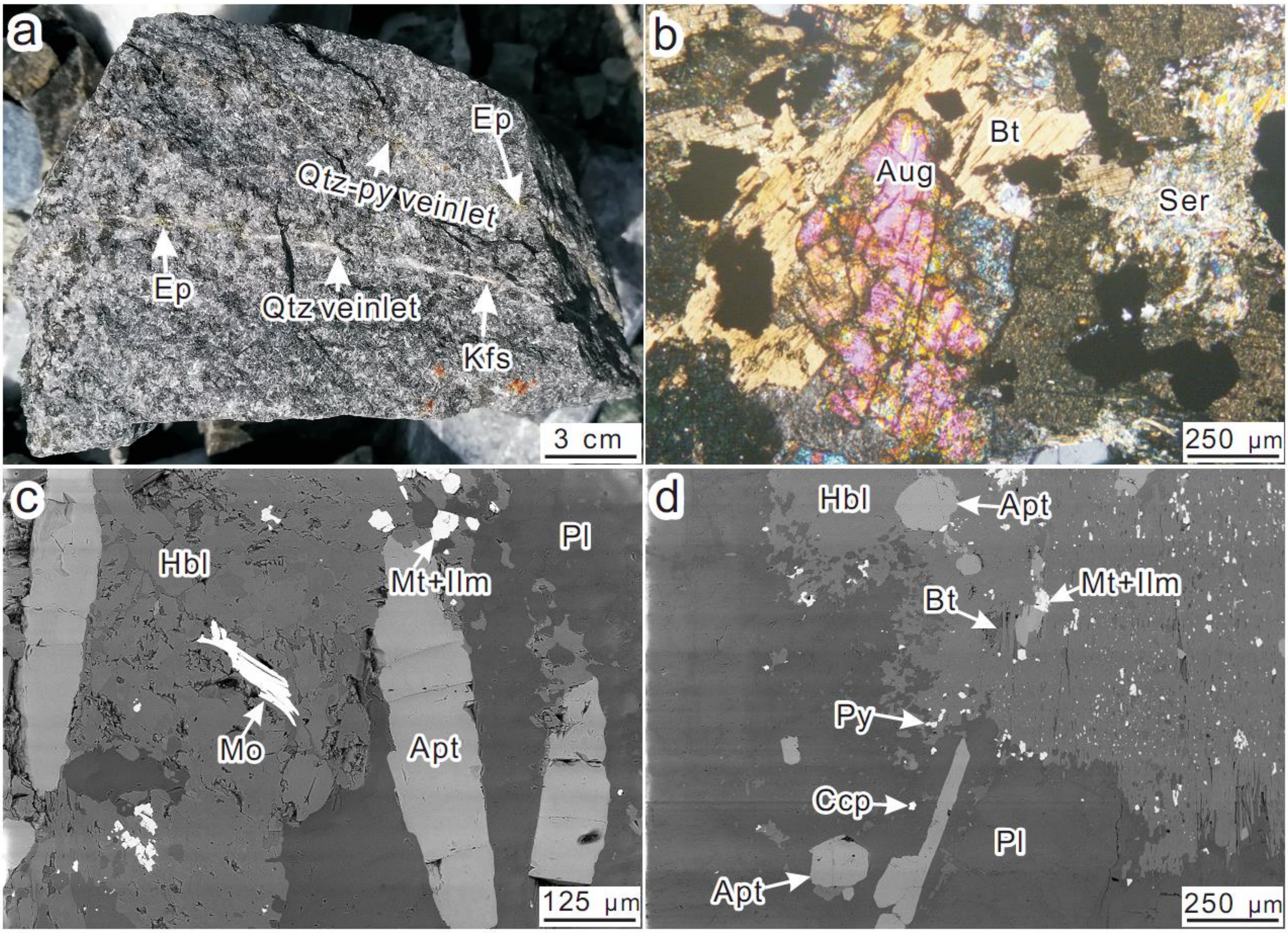
a
Ep
Qtz-py veinlet
Ep
Qtz veinlet
Kfs
3 cm
b
Bt
Aug
Ser
250 μm
c
Hbl
Pl
Mt+Ilm
Mo
Apt
125 μm
d
Hbl
Apt
Mt+Ilm
Bt
Py
Ccp
Pl
Apt
250 μm

Figure 7

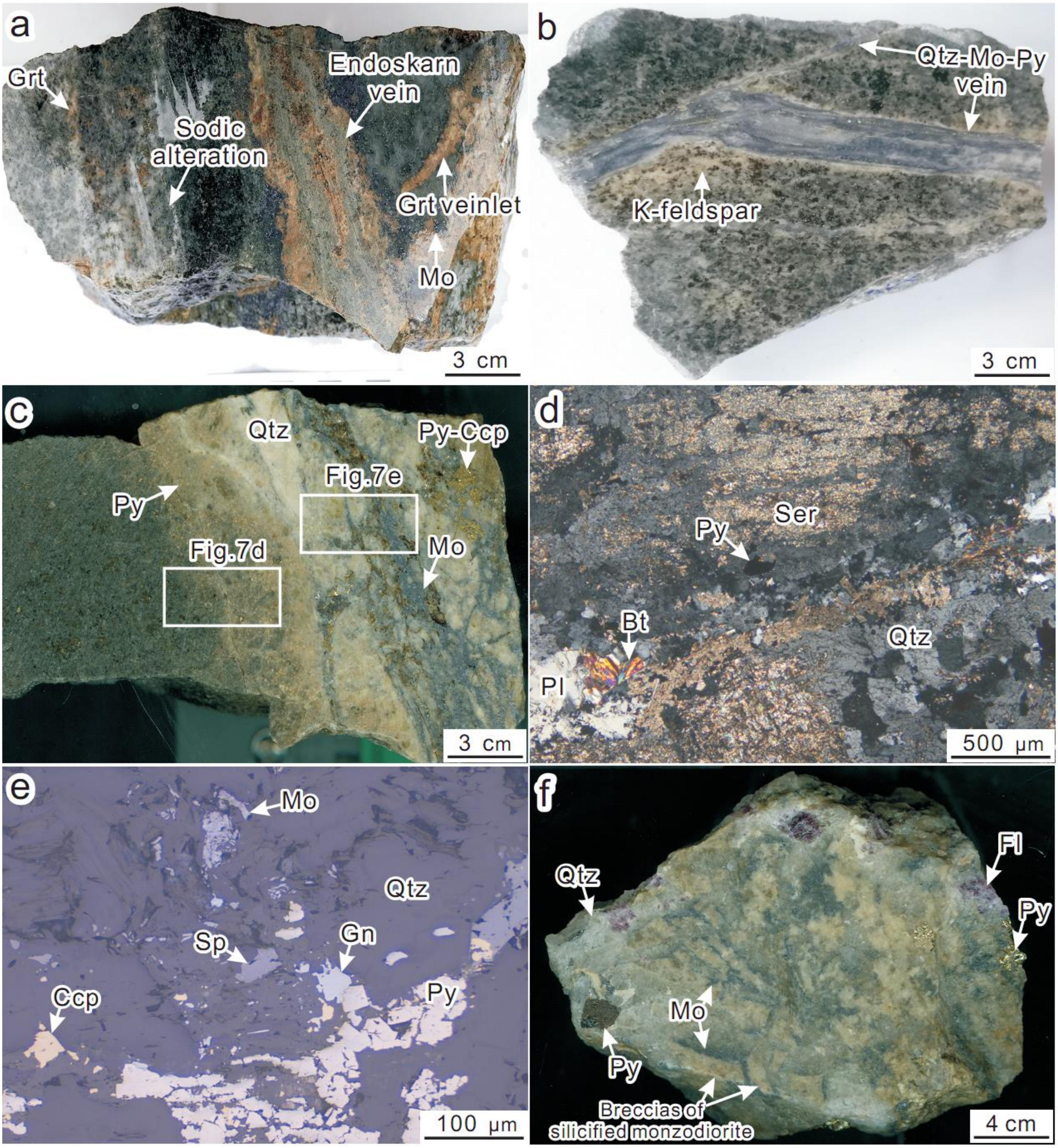
a
Grt
Sodic
alteration
Endoskarn
vein
Grt veinlet
Mo
3 cm
b
Qtz-Mo-Py
vein
K-feldspar
3 cm
c
Qtz
Py-Ccp
Fig.7e
Py
Fig.7d
Mo
3 cm
d
Ser
Py
Bt
Qtz
Pl
500 μm
e
Mo
Qtz
Sp
Gn
Ccp
Py
100 μm
f
Fl
Qtz
Py
Mo
Py
Breccias of
silicified monzodiorite
4 cm

Figure 8

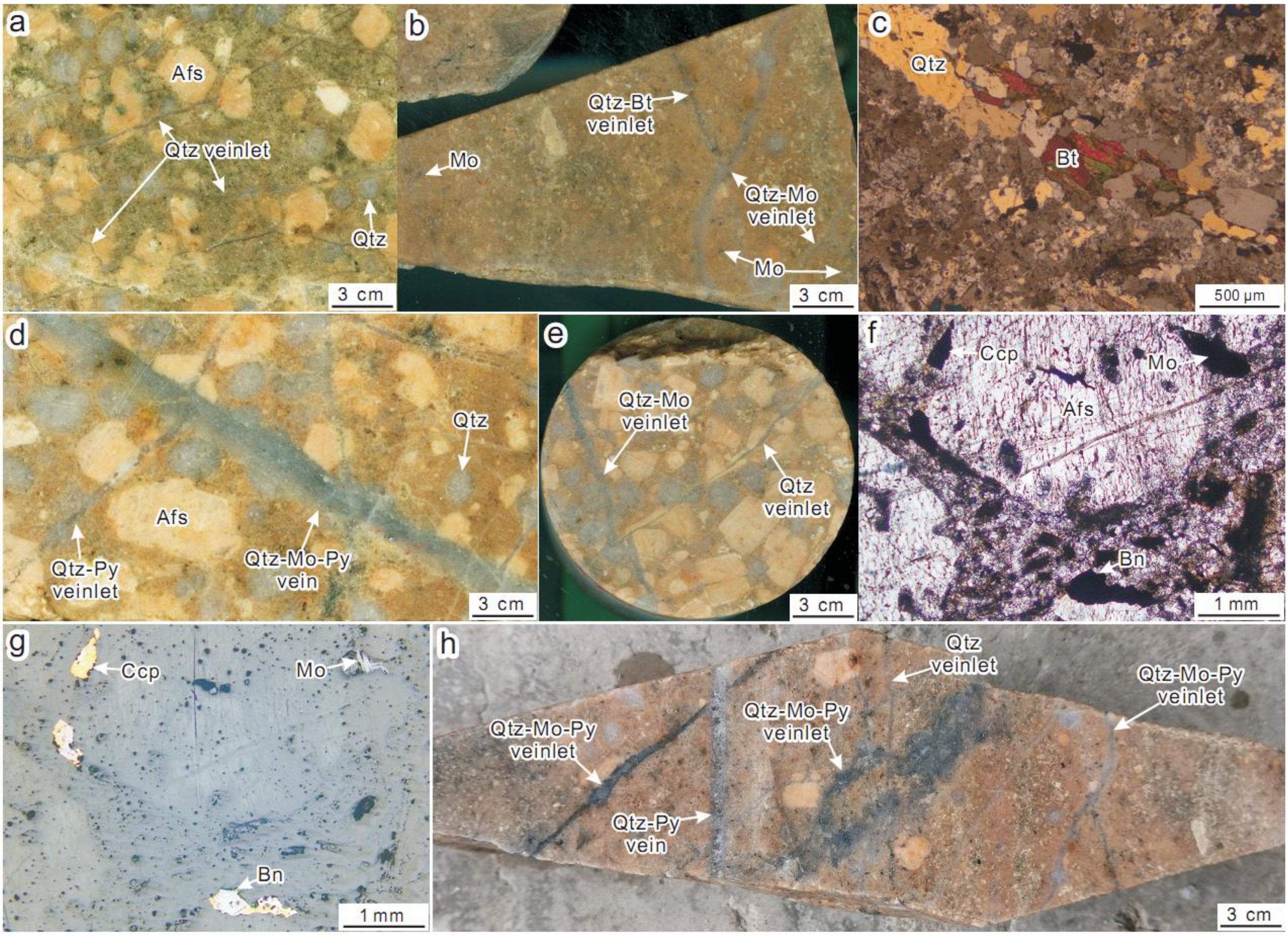
a
Afs
Qtz veinlet
Qtz
3 cm
b
Qtz-Bt
veinlet
Mo
Qtz-Mo
veinlet
Mo
3 cm
c
Qtz
Bt
500 μm
d
Qtz
Afs
Qtz-Py
veinlet
Qtz-Mo-Py
vein
3 cm
e
Qtz-Mo
veinlet
Qtz
veinlet
3 cm
f
Ccp
Mo
Afs
Bn
1 mm
g
Ccp
Mo
Bn
1 mm
h
Qtz
veinlet
Qtz-Mo-Py
veinlet
Qtz-Mo-Py
veinlet
Qtz-Mo-Py
veinlet
Qtz-Py
vein
3 cm

Figure 9

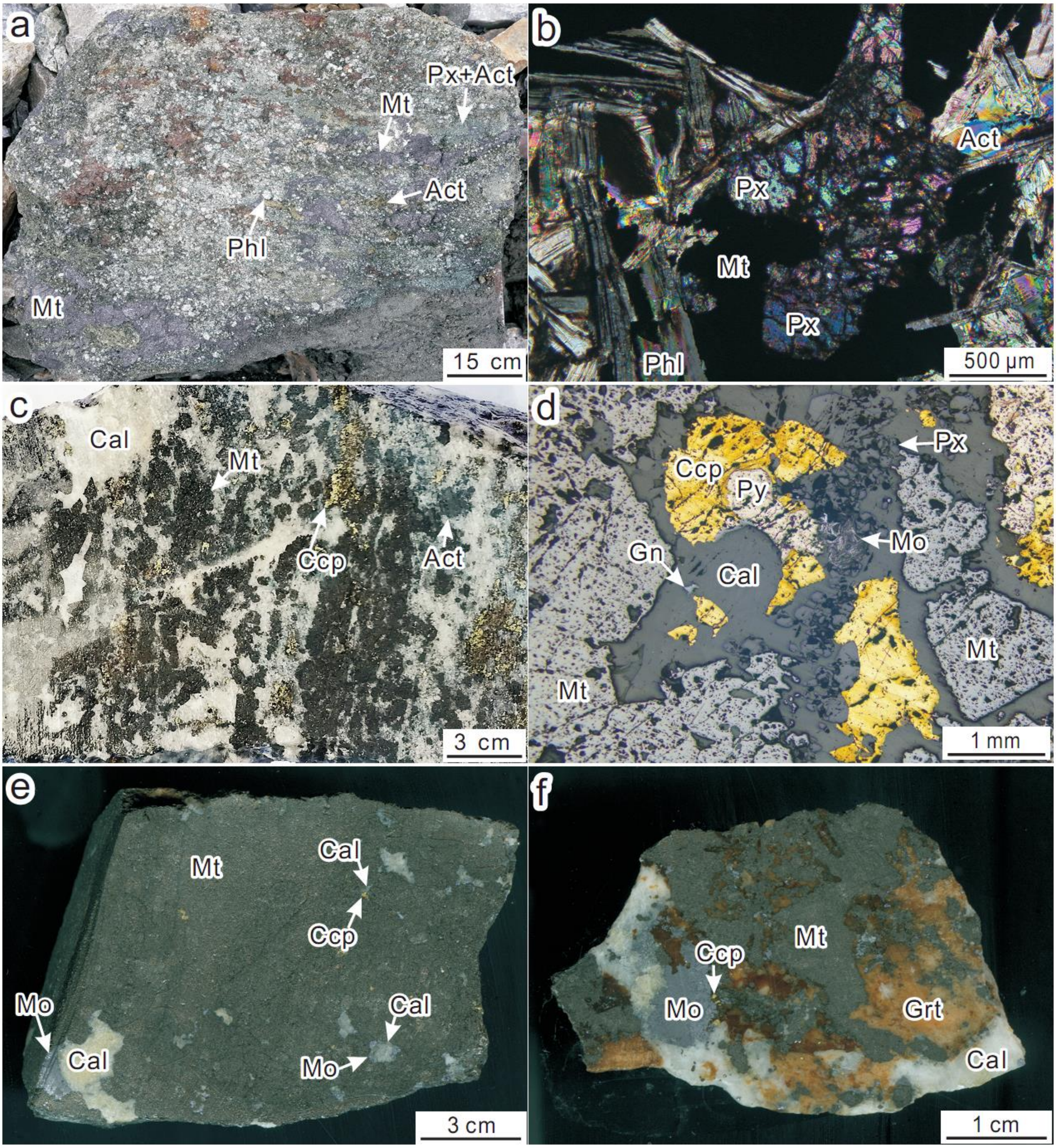

a
Px+Act
Mt
Act
Phl
Mt
15 cm
b
Act
Px
Mt
Px
Phl
500 μm
c
Cal
Mt
Ccp
Act
3 cm
d
Px
Ccp
Py
Mo
Gn
Cal
Mt
Mt
1 mm
e
Mt
Cal
Ccp
Cal
Mo
Cal
Mo
3 cm
f
Mt
Ccp
Mo
Grt
Cal
1 cm

Figure 10

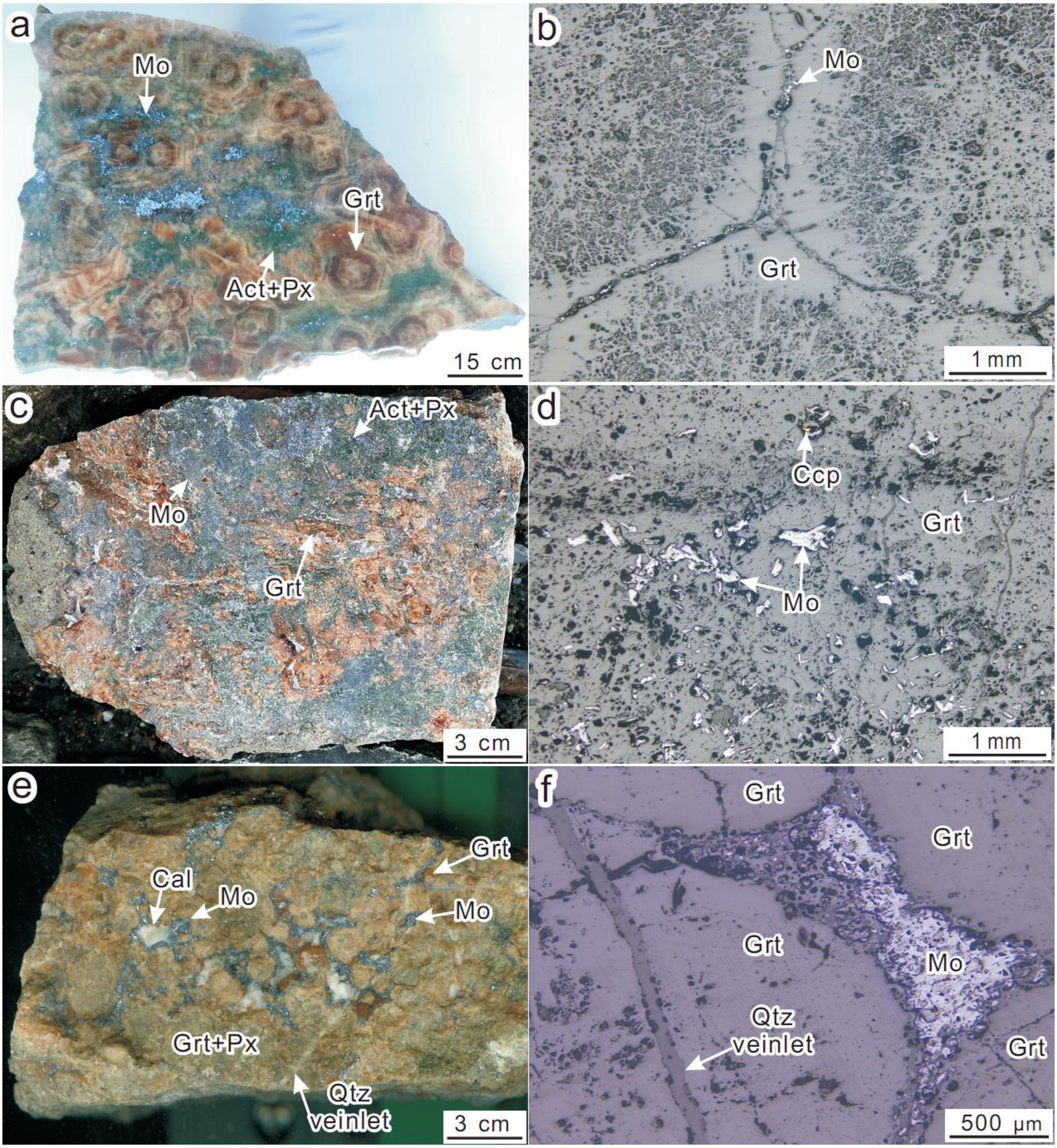
a
Mo
Grt
Act+Px
15 cm
b
Mo
Grt
1 mm
c
Act+Px
Mo
Grt
3 cm
d
Ccp
Grt
Mo
1 mm
e
Grt
Cal
Mo
Mo
Grt+Px
Qtz
veinlet
3 cm
f
Grt
Grt
Grt
Mo
Qtz
veinlet
Grt
500 μm

Figure 11

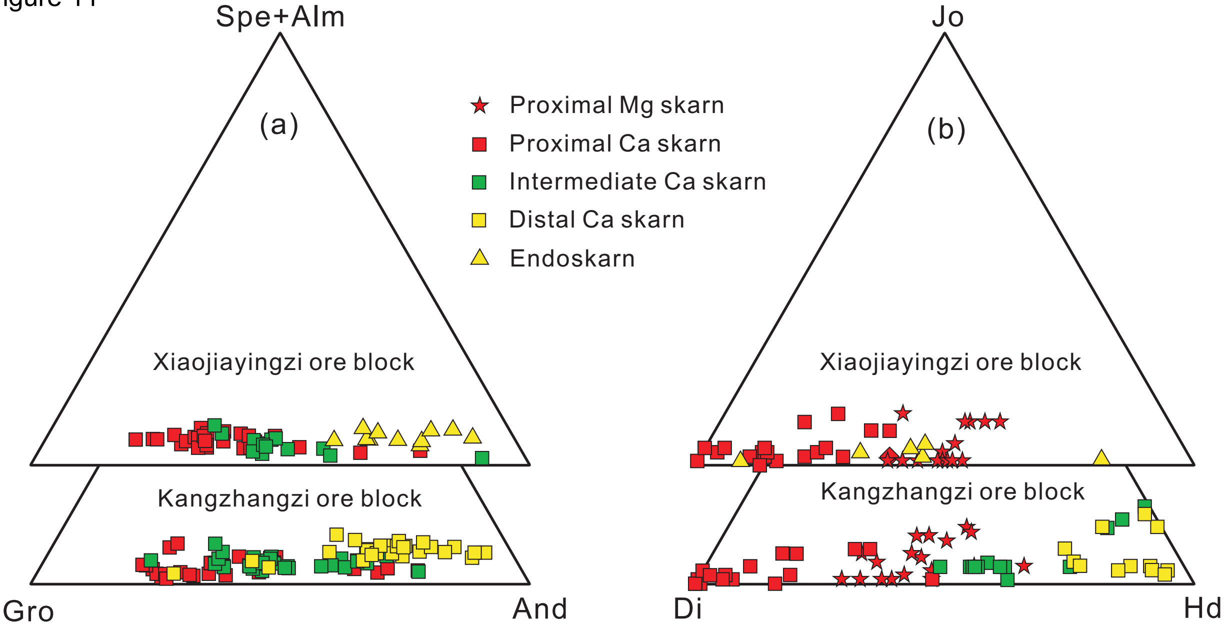

Spe+Alm
(a)
Xiaojiayingzi ore block
Kangzhangzi ore block
Gro
And
Jo
(b)
Xiaojiayingzi ore block
Kangzhangzi ore block
Di
Hd
Proximal Mg skarn
Proximal Ca skarn
Intermediate Ca skarn
Distal Ca skarn
Endoskarn

Figure 12

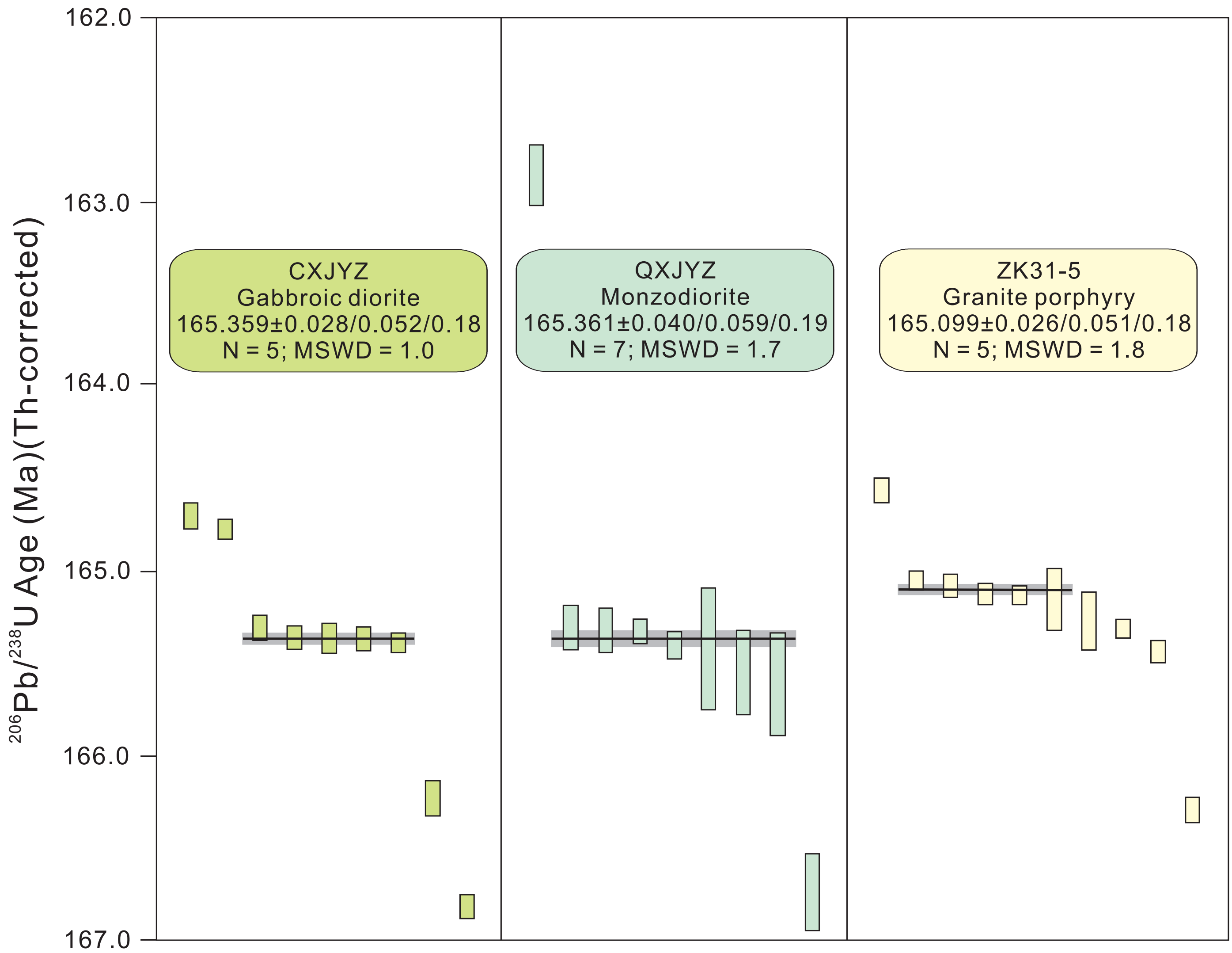
162.0
163.0
164.0
165.0
166.0
167.0
206Pb/238U Age (Ma)(Th-corrected)
CXJYZ
Gabbroic diorite
165.359±0.028/0.052/0.18
N = 5; MSWD = 1.0
QXJYZ
Monzodiorite
165.361±0.040/0.059/0.19
N = 7; MSWD = 1.7
ZK31-5
Granite porphyry
165.099±0.026/0.051/0.18
N = 5; MSWD = 1.8

Figure 13

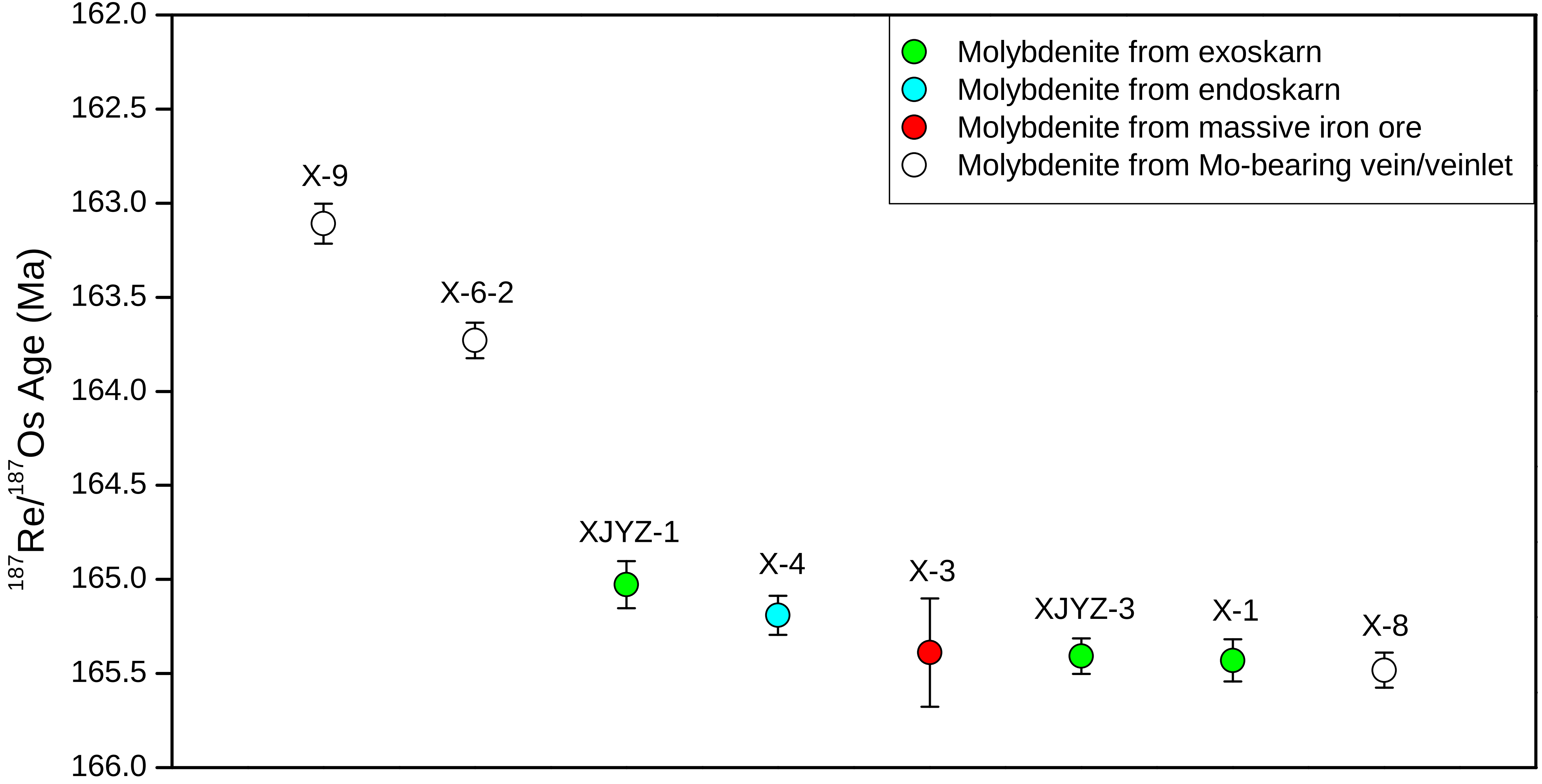

162.0
162.5
163.0
163.5
164.0
164.5
165.0
165.5
166.0
^{187}Re/^{187}Os Age (Ma)
X-9
X-6-2
XJYZ-1
X-4
X-3
XJYZ-3
X-1
X-8
Molybdenite from exoskarn
Molybdenite from endoskarn
Molybdenite from massive iron ore
Molybdenite from Mo-bearing vein/veinlet

Figure 14

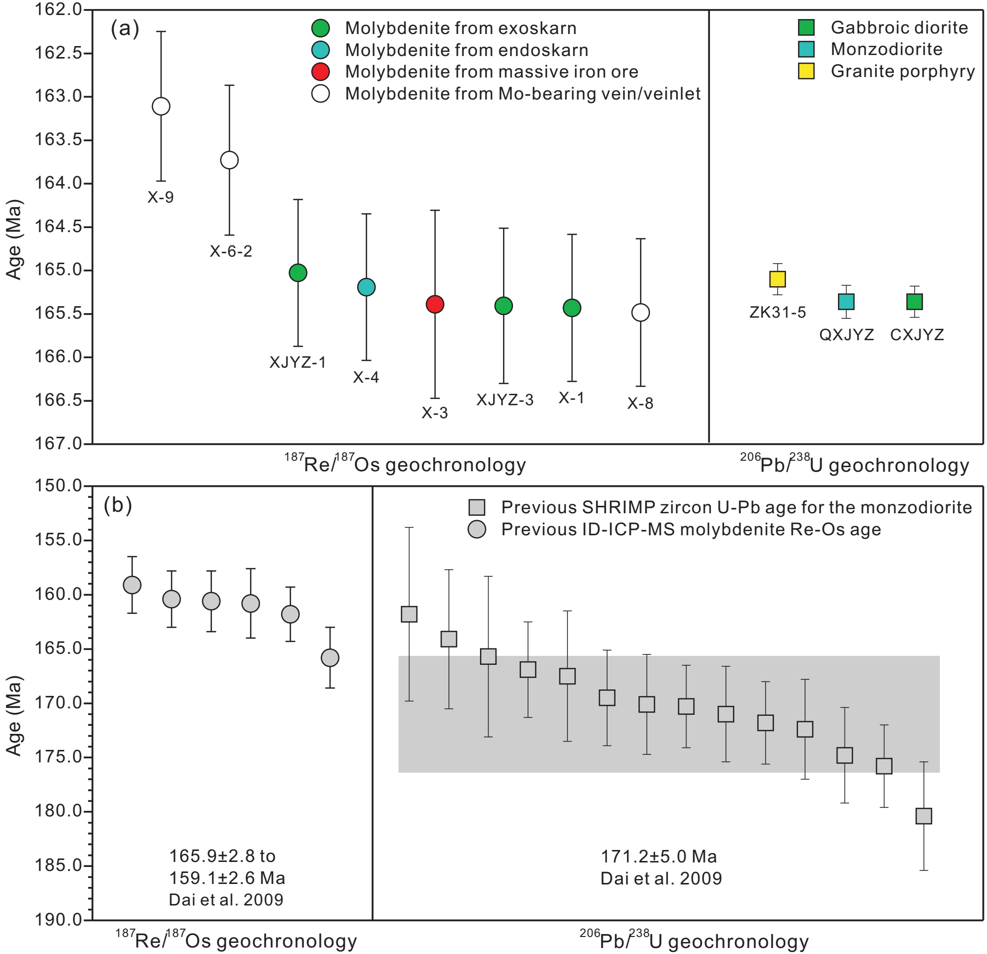

(a)
Age (Ma)
162.0
162.5
163.0
163.5
164.0
164.5
165.0
165.5
166.0
166.5
167.0
Molybdenite from exoskarn
Molybdenite from endoskarn
Molybdenite from massive iron ore
Molybdenite from Mo-bearing vein/veinlet
X-9
X-6-2
XJYZ-1
X-4
X-3
XJYZ-3
X-1
X-8
Gabbroic diorite
Monzodiorite
Granite porphyry
ZK31-5
QXJYZ
CXJYZ
187Re/187Os geochronology
206Pb/238U geochronology
(b)
Age (Ma)
150.0
155.0
160.0
165.0
170.0
175.0
180.0
185.0
190.0
Previous SHRIMP zircon U-Pb age for the monzodiorite
Previous ID-ICP-MS molybdenite Re-Os age
165.9±2.8 to
159.1±2.6 Ma
Dai et al. 2009
171.2±5.0 Ma
Dai et al. 2009
187Re/187Os geochronology
206Pb/238U geochronology

Figure 15

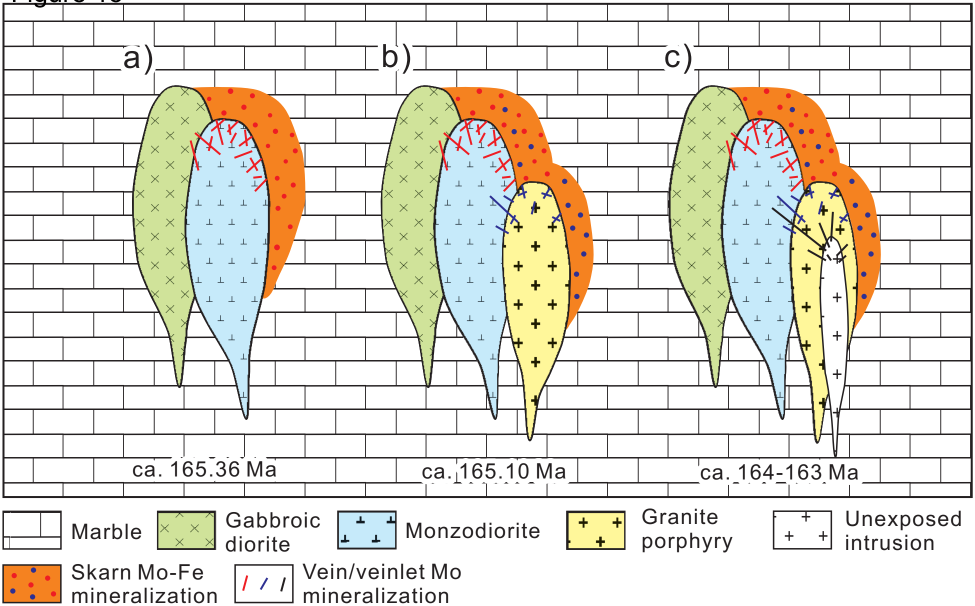

a)
b)
c)
ca. 165.36 Ma
ca. 165.10 Ma
ca. 164-163 Ma
Marble
Gabbroic diorite
Monzodiorite
Granite porphyry
Unexposed intrusion
Skarn Mo-Fe mineralization
Vein/veinlet Mo mineralization

Table 1 Distinctive features of intrusions at Xiaojiayingzi

Intrusion	Texture	Rock-forming mineral (vol. %)*		Accessory minerals	Crosscutting relationships	Veining (vol. %)	Observed vein/veinlets	Alteration	Mineralization
		Phenocryst	Groundmass						
Gabbroic diorite	Coarse - grained	Pl:55-65% (0.5-3 mm); Bt:10-15% (0.5-1 mm); Hbl:5-10% (0.5-0.8 mm); Aug:5-10% (0.5-1 mm)	nil	Apatite, ilmenite, magnetite, titanite, and zircon		< 2 %	Quartz - K-feldspar, quartz - pyrite ± ganela ± sphalerite ± chalcopyrite, and molybdenite	Weak to moderate K-feldspar and sericitic	Weak
Monzodiorite	Medium - grained to porphyritic	Pl:50-60% (0.2-10 mm); Afs:10-15% (0.1-0.5 mm); Bt:10-15% (0.1-0.4 mm); Hbl:5-10% (0.1-0.3 mm); Qtz:<5% (0.1-0.3 mm); Aug:<1% (0.3-0.5 mm)	nil	Apatite, ilmenite, magnetite, titanite, and zircon	Intrude gabbroic monzodiorite	5 - 10 %	Endoskarn, quartz - molybdenite-pyrite, and quartz – molybdenite - pyrite - chalcopyrite – galena - sphalerite	Weak to intense sodic, K-feldspar, sericitic and skarnization	Intense
Granite porphyry	Porphyritic	Afs:30-40% (5-30 mm); Qtz:10-15% (1-10 mm); Pl:<5% (1-3 mm); Bt:<1% (0.5-0.6 mm)	Qtz:30-35% (0.01-0.2 mm); Afs:~5% (0.01-0.05 mm) ; Pl:<2% (0.1-0.2 mm); Bt:<2% (0.02-0.05 mm)	Zircon, apatite, and magnetite	Intrude gabbroic diorite and monzodiorite	2 - 5 %	Quartz, quartz – biotite, quartz - molybdenite - pyrite, and quartz - pyrite	Weak to intense K-silicate and sericitic	Weak to moderate

* Mineral abundance is estimated from least-altered samples of each intrusion

Abbreviations: Bt = biotite, Aug = augite, Hbl = hornblende, Afs = alkaline feldspar, Ilm = ilmenite, Mag = magnetite, Pl = plagioclase, Qtz = quartz

Table 2 Molybdenite Re-Os data of the samples from the Xiaojiayingzi deposit

Sample	Sample description	wt (g)	Re (ppm)	±2σ	^{187}Re (ppm)	±2σ	^{187}Os (ppb)	±2σ	Age (Ma)	±^	±*	±#
X-8	Quartz - molybdenite - pyrite - chalcopyrite - galena - sphalerite vein in silicified monzodiorite	0.0105	72.0	0.4	45.2	0.2	124.9	0.6	165.48	0.09	0.68	0.85
X-1	Massive exoskarn consists mainly of garnet with less amount of pyroxene overprinted by molybdenite, calcite, actinolite, pyrite, and chalcopyrite	0.0104	101.2	0.5	63.6	0.3	175.5	0.8	165.43	0.11	0.67	0.85
XJYZ-3	Massive exoskarn consists mainly of garnet with less amount of pyroxene overprinted by molybdenite, calcite, actinolite, pyrite, and chalcopyrite	0.0204	13.5	0.1	8.5	0.0	23.5	0.1	165.41	0.09	0.73	0.89
X-3	Massive iron ore consists mainly of garnet and magnetite, which was in turn overprinted by molybdentie, calcite, pyrite, and chalcopyrite	0.1017	0.3	0.0	0.2	0.0	0.5	0.0	165.39	0.29	0.95	1.08
X-4	Molybdenite-bearing endoskarn. The monzodiorite was metasomatized into endoskarn partially and was in turn overprinted by molybdenite and pyrite	0.0103	114.0	0.6	71.6	0.4	197.4	0.9	165.19	0.10	0.67	0.84
XJYZ-1	Massive exoskarn consists mainly of garnet with less amount of pyroxene overprinted by molybdenite, calcite, actinolite, pyrite, and chalcopyrite	0.0108	79.6	0.4	50.0	0.2	137.7	0.6	165.03	0.13	0.67	0.85
X-6-2	Quartz-molybdenite-pyrite veinlets in granite porphyry	0.0140	26.1	0.1	16.4	0.1	44.8	0.2	163.73	0.09	0.70	0.86
X-9	Quartz-molybdenite- pyrite vein in monzodiorite with K-feldspar haloes	0.0065	47.7	0.3	30.0	0.2	81.5	0.5	163.11	0.11	0.70	0.86

^uncertainty including only mass spectrometry uncertainty

*uncertainty including all sources of analytical uncertainty

#uncertainty including all sources of analytical uncertainty plus decay constant

Appendix Table S1 descriptions of the samples

Click here to access/download
Electronic Appendix (Excel etc.)
Appendix Table S1 descriptions of the samples.xls

Click here to access/download
Electronic Appendix (Excel etc.)
Appendix Table S2 molybdenite dating samples.xls